

An Empirical Study of Remote Sensing Pretraining

Di Wang, Jing Zhang, Bo Du, *Senior Member, IEEE*, Gui-Song Xia, *Senior Member, IEEE*,
and Dacheng Tao, *Fellow, IEEE*

Abstract—Deep learning has largely reshaped remote sensing research for aerial image understanding. Nevertheless, most of existing deep models are initialized with ImageNet pretrained weights, where the natural images inevitably presents a large domain gap relative to the aerial images, probably limiting the finetuning performance on downstream aerial scene tasks. This issue motivates us to conduct an empirical study of remote sensing pretraining (RSP). To this end, we train different networks from scratch with the help of the largest remote sensing scene recognition dataset up to now-MillionAID, to obtain the remote sensing pretrained backbones, including both convolutional neural networks (CNN) and vision transformers such as Swin and ViTAE, which have shown promising performance on computer vision tasks. Then, we investigate the impact of ImageNet pretraining (IMP) and RSP on a series of downstream tasks including scene recognition, semantic segmentation, object detection, and change detection using the CNN and vision transformers backbones. We have some empirical findings as follows. First, vision transformers generally outperforms CNN backbones, where ViTAE achieves the best performance, owing to its strong representation capacity by introducing intrinsic inductive bias from convolutions to transformers. Second, both IMP and RSP help deliver better performance, where IMP enjoys a versatility by learning more universal representations from diverse images belonging to much more categories while RSP is distinctive in perceiving remote sensing related semantics. Third, RSP mitigates the data discrepancy of IMP for remote sensing but may still suffer from the task discrepancy, where downstream tasks require different representations from the scene recognition task. These findings call for further research efforts on both large-scale pretraining datasets and effective pretraining methods. The codes and pretrained models will be released at <https://github.com/ViTAE-Transformer/ViTAE-Transformer-Remote-Sensing>.

Index Terms—Remote Sening Pretraining, CNN, Vision Transformer, Classification, Detection, Semantic Segmentation.

I. INTRODUCTION

With the development of geoinformatics technology, the earth observation fields have witnessed significant progress, where various remote sensing sensors and devices have been widely used. Among them, with the advantages of real-time, abundant amount and easy-acquiring, the aerial image has become one of the most important data sources in earth vision to serve for the requirements of a series of practical tasks, such as precision agriculture [1], [2] and environmental monitoring [3]. In these applications, the aerial scene recognition is a fundamental and active research topic

D. Wang, B. Du and Gui-Song Xia are with the School of Computer Science, Wuhan University, Wuhan 430072, China (e-mail: wd74108520@gmail.com; dubo@whu.edu.cn; guisong.xia@whu.edu.cn). B. Du is the corresponding author.

J. Zhang is with the School of Computer Science, Faculty of Engineering, The University of Sydney, Australia (jing.zhang1@sydney.edu.au).

D. Tao is with the JD Explore Academy, China (dacheng.tao@gmail.com).

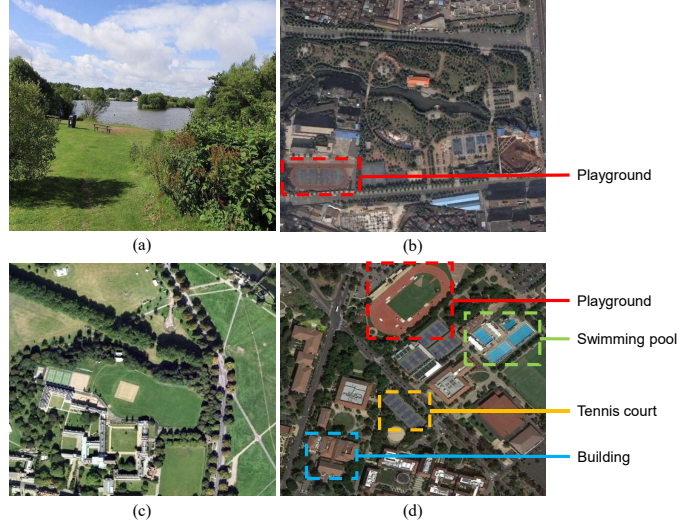


Fig. 1. The challenges of aerial scene recognition. (a) and (b) are the natural image and aerial image belonging to the “park” category. (c) and (d) are two aerial images from the “school” category. Despite the distinct view difference of (a) and (b), (b) contains the playground that is unusual in the park scenes but usually exists in the school scenes like (d). On the other hand, (c) and (d) show different colors as well as significantly different spatial distributions of land objects like playground and swimming pool.

over the past years. However, because of the own characteristics of aerial images, it is still challenging to efficiently understand the aerial scene.

The aerial images are usually obtained by a camera in a bird-view perspective lying on the planes or satellites, perceiving a large scope of land uses and land covers. The obtained aerial scene is usually difficult to be interpreted since the interference of the scene-irrelevant regions and the complicated spatial distribution of land objects. Specifically, it causes the issue of inter-class similarity in aerial scene understanding, i.e., some different scenes present similar characteristics, as well as the issue of large intra-class variations, where the scenes in a same category have discrepancies, as shown in Figure 1.

In order to tackle above problems, it is necessary to obtain discriminative feature representations for different categories of aerial scenes. According to the difference of feature extraction methods, they can be divided into three types, i.e., the handcrafted features, the unsupervised learning features and the supervised deep learning features. In the early works of aerial scene recognition, researchers directly utilize the simple properties, such as color [4], texture [5], contour [6], spectral or their combination [7] to distinguish different aerial scenes. Besides these intuitive attributes, there are also some well-designed feature descriptors. For instance, the scale-invariant feature transformation and histogram of oriented gradients.

These handcrafted features usually perform well in simple scenes while being ineffective in complex scenes. They are usually regarded as shallow features from a modern view in the deep learning era, while interpreting complex scenes requires more semantic information, which can not be efficiently extracted by shallow-layer methods [8]. Compared with the above approaches, the unsupervised learning methods provide a feasible way to automatically extract the suitable features by adaptively learning the mapping functions or filters based on a set of handcrafted features or the raw pixel intensity values. The typical unsupervised learning methods include potential latent semantic analysis [9] and bag of visual words [10]. In fact, some simple feature enhancement methods such as the principal component analysis also belong to this category. Nonetheless, the encoded unsupervised features still have limited performance since no category supervision is explicitly used, which is useful for feature discrimination.

In recent years, with the superiority of automatically extracting deep features that reflect the inherent properties of objects, deep learning has achieved an impressive break through in the computer vision field [11]–[17], as well as the remote sensing field [18]–[20]. In the aerial scene recognition domain, the most commonly used deep models are the convolutional neural networks (CNN), which have a good ability of local perception and global perception, where the former is achieved via applying sliding window convolutions on the input image to extract the local features while the latter is achieved by stacking multiple convolutional layers to increase the receptive field. According to the training scheme, the ways of using CNN in aerial scene recognition methods can be divided into three categories, i.e., training from scratch, finetuning, and adoption as the feature extractor. The first scheme does not involve any external data, meaning there is no prior knowledge that can be leveraged. To remedy this issue, the finetuning scheme uses the networks pretrained on a large-scale dataset as the start point for further training (i.e., finetuning). The last scheme directly extracts the feature from the pretrained CNN without further finetuning, therefore lacking of the flexibility of adapting to aerial images from different downstream tasks.

The existing literatures [21] reveal that the finetuning strategy performs better than the other ones. We attribute it to the capacity of the used pretraining dataset, including the sample size and the number of category. In the current remote sensing field including the aerial scene recognition task, almost all finetuned models are pretrained on the ImageNet-1K dataset [22], which is the most famous image dataset in the computer vision field. Its millions of real-world images from 1,000 different categories enable the models to learn a powerful representation. Usually, off-the-shelf deep models like VGG [11] and ResNet [12] are used as backbone networks for aerial scene recognition, since training a new network on the ImageNet from scratch is time-consuming and requires a large amount of computational resources. In order to further improve the classification performance, some methods [23], [24] adopt the ImageNet pretrained models as the backbone network and employ multi-level features from it. In addition, many other components or strategies are specially designed for the aerial recognition task, such as the distillation [25] and

feature partitioning [26].

Although the aforementioned methods have achieved remarkable performance for aerial scene recognition, there are still some issues needed to be further investigated. Intuitively, when considering the characteristics of aerial images, there obviously exists a large domain gap compared with the natural images in terms of view, color, texture, layout, object, etc. Previous methods attempt to narrow this gap by further finetuning the pretrained model on the remote sensing image dataset. Nevertheless, the systematic bias introduced by ImageNet Pretraining (IMP) has a non-negligible side impact on the performance. On the other hand, we notice that there are abundant aerial images captured by diverse multiple sensors with the progress of remote sensing technology, which can be used for pretraining. As a representative example, MillionAID [27] is so far the largest aerial image dataset, which is collected from the Google Earth images captured by diverse sensors and also has a million-level volume similar to ImageNet-1K, making the Remote Sensing Pretraining (RSP) become possible.

RSP enables to train a deep model from scratch, implying that the candidate model is not necessary to be limited to the off-the-shelf CNN. In this paper, we also investigate the impact of RSP together with vision transformers, which have shown surprising good performance in the computer vision domain. Compared with convolutions in CNN which is skilled in modelling locality, the multi-head self-attention (MHSA) in transformers, e.g., Swin transformer [13], is able to flexibly capture diverse global context. Recently, ViTAE [14], [28] explores both convolutions and MHSA for modelling locality and long-range dependency simultaneously, achieving state-of-the-art performance on the ImageNet classification task and downstream vision tasks. In addition, it also extracts multi-scale features through a dilated convolution module and the stage-wise design, which have been shown effective in previous works, especially for aerial image interpretation [29]. Since both the CNN and aforementioned vision transformers can also produce intermediate features in different stages, which are useful for many downstream tasks, we also investigate the finetuning performance of them after RSP on semantic segmentation, object detection, and change detection. To achieve these goals, we conduct extensive experiments on nine popular datasets and have some findings. The RSP is an emerging research direction in aerial image understanding, which however is still under-explored, especially in the context of vision transformers. We hope this study could fill this gap and provide useful insights for future research.

The main contribution of this paper is four-fold.

- (1) We discuss the deficiency of the commonly used ImageNet pretraining in the aerial image understanding area and the motivation of the remote sensing pretraining.
- (2) We investigate the impact of remote sensing pretraining on three kinds of backbone networks, including the conventional CNN, the competitive vision transformer model, and the advanced ViTAE transformer, by pretraining them on the large-scale remote sensing dataset.
- (3) We further finetune the above models that are initialized with the remote sensing or ImageNet pretraining weights

on four kinds of tasks including scene recognition, semantic segmentation, object detection, and change detection using a total of nine datasets, and compare them with other state-of-the-art (SOTA) methods.

- (4) The experimental results show that, 1) the typical vision transformer models can obtain competitive performance or perform better than CNN on the four tasks, especially, the ViTAE achieves the best performances on almost all settings even if compared with the SOTA methods; 2) the remote sensing pretraining achieves surprising good performance on the scene recognition task, and has advantages on specific categories such the “Bridge” on segmentation and detection tasks compared to the ImageNet pretraining; and 3) We also find that the performances of remote sensing pretraining are affected by the type of task, revealing the issue of representation similarity and providing insights to the future research.

The remainder of this paper is organized as follows. Section II introduces the related works, including the aerial scene recognition methods, especially CNN and vision transformer related ones, and the existing works of RSP. Section III describes the implementations of RSP, as well as the employed large capacity MillionAID dataset and the adopted ViTAE network. The experiments results on the four tasks and the related comprehensive analyses are presented in section IV. Finally, Section V concludes this paper.

II. RELATED WORK

A. Aerial Scene Recognition

There are large number of CNN-based approaches on aerial scene recognition. Many off-the-shelf CNN classification models that are pretrained on ImageNet, such as the VGG [11], ResNet [12], and DenseNet [30], have been used and further finetuned on aerial images. Nonetheless, the challenging aerial scene that possesses inter-class similarity and intra-class diversity can not be easily interpreted by only using features of the last layer, which are also considered as the “global features” compared with the features in previous layers, since it is also useful to highlight the important scene-relevant local regions for scene understanding. To address this issue, [23], [31] jointly exploits the multi-level CNN features, where the high-level features from deep layers usually have abundant semantic information, while the low-level features of the shallow layers tend to provide visual structures. For example, [31] conducts varied dilated convolutions on multiple features of VGG to obtain the more effective multiscale features. In addition, they optimize the category probabilities by preserving the local maximum and revising others with the two-dimensional Gaussian-like distribution in a window to strengthen the local regions. [23] separately applies graph convolutions on multilayer VGG features, where each pixel representation is regarded as a node, and the extracted graph features are concatenated with the last global visual features.

Apart from feature fusion, the attention mechanisms have also been commonly used in aerial scene recognition since they can enhance the local features by simulating the human

vision that directly assigns different weights on various areas of current scene. The attention modules can be easily inserted into the CNN [32]. For example, [33] adopts channel attention and spatial attention modules in parallel like [34] to form a complementary attention. [31] also employs the spatial attention to further adjust the optimized category probabilities. Another point for aerial scene recognition is to model the relationships of different regions. For example, [23] captures the topological relations of different objects, where the adjacency matrices are carefully designed. Besides, some interesting topics such as the multiple instance learning [35], self-distillation [25] and feature partition [26] have also been explored in aerial scene recognition research.

B. Vision Transformer

The recently proposed vision transformers inspire a wave of researches [13], [14], [28], [36]–[43] in computer vision fields and achieve superior performance than CNN. The core component of vision transformer is the MHSAs, which is the extension of the self-attention (SA). Compared with the convolution operation, the SA has the ability of capturing long-range context and the relationships between any different positions. On the foundation of SA, the MHSAs separately conducts the SAs in different projected subspaces, possessing a more powerful representative abilities. ViT [36] is the pioneer vision transformer, where the input image is split into fixed size patches to form tokens, which are then fed into the MHSAs. However, the fixed receptive field restricts its applications on downstream tasks, and the globalMHSAs brings high computational complexities. To address the former issue, PVT [38] adopts the classical pyramid structure, improving the model transferability with the generated hierarchical multiscale features. Swin [13] further substitutes the global MHSAs to the shiftable window MHSAs (WMHSAs), it reduces the computational overhead significantly, achieving excellent performance on many computer vision tasks. Nonetheless, it still suffers from the common issues of vision transformers, such as being inefficient in modeling locality and scale invariance, which are exactly the advantages of CNN. Thus, besides Swin, we also employ another advanced vision transformer named ViTAE [14], [28], where the intrinsic biases of CNN are introduced into the transformer. It also adopts a pyramid structure to generate hierarchical features and local window attention, achieving better performance on many computer vision tasks while having a reasonable computational overhead and memory footprint. Using vision transformers as the backbone for aerial scene recognition is still under-explored, while the existing method merely takes ViT as a branch parallel to CNN [44], implying an urgent need to further explore the applications of vision transformers on aerial scene tasks.

C. Remote Sensing Pretraining

Pretraining using remote sensing dataset for aerial scene recognition is a very intuitive idea. However, to our best knowledge, there is little exploration in this direction since the insufficiency of large-scale remote sensing datasets like ImageNet. Nevertheless, researchers have attempted to obtain

the remote sensing representations from other resources. For example, GeoKR [45] leverages the global land cover product as the labels, and they use the mean-teacher framework to alleviate the influences of imaging time and resolution discrepancies between remote sensing images and geographical ones. However, forcing alignment of different datasets inevitably brings errors due to the intrinsic different data distributions. In fact, the scarcity of large capacity remote sensing dataset is mainly in the aspect of category labels instead of images. In this case, it is promising to develop self-supervised pretraining methods [46]–[49] and some related methods have been developed in the remote sensing area [50]–[53]. For instance, SeCo [50] leverages the seasonal changes to enforce consistency between positive samples, which are the unique characteristics in aerial scenes, while [52] simultaneously fuses the temporal information and geographical location into the MoCo-V2 [47] framework. Moreover, the channel properties [53] and spatial variance [51] are also explored in some approaches. In this study, since the adopted MillionAID dataset has the ground truth labels annotated by experts and dose not contain any temporal information, we directly conduct the supervised pretraining like the conventional IMP.

III. REMOTE SENSING PRETRAINING

In this section, we first provide a brief introduction of the adopted large-scale remote sensing dataset—MillionAID. Then, we describe the details of the utilized ViTAE transformer. The whole RSP procedure will be presented finally.

A. MillionAID

To our best knowledge, the MillionAID is by far the largest dataset in the remote sensing area. It contains 100,0848 non-overlapping scenes, exceeding the competitive counterpart fMoW [54] and BigEarthNet [55], which separately includes 132,716 and 590,326 scenes. Note that the fMoW actually contains 1,047,691 images, since they provide multiple temporal views for each scene. In addition, it should be noted that the fMoW and BigEarthNet are multispectral dataset, while the MillionAID is a RGB dataset, which is more suitable for existing deep vision models. The categories of MillionAID consist a hierarchical tree that has 51 leaves, which locate on 28 parent nodes on the second level, while the 28 groups are belonging to 8 base classes: agriculture land, commercial land, industrial land, public service land, residential land, transportation land, unutilized land and water area, and each leaf category has about 2,000~45,000 images. This dataset is obtained from the Google Earth (GE) that is made up of diversity sensors including but not limited to SPOT, IKONOS, WorldView and Landsat series, resulting in different resolutions. The maximum resolution can reach 0.5m, while the smallest is 153m. The image size ranges from 110 × 110 to 31,672 × 31,672.

B. ViTAE

The original ViTAE [14] follows the deep-narrow design of T2T-ViT [56], which found that simply decreasing channel

dimensions and increasing layer depth can improve the feature richness of ViT, boosting the performance while reducing the model size and computational cost. Thus, the original ViTAE firstly downsamples the input image to 1/16 size by three reduction cells. Similar to ViT, a class token is concatenated with the output of the third reduction cell before adding an element-wise sinusoid position encoding. Then, multiple normal cells are stacked, and the feature size is always kept till the end. The class token feature of the last normal cell is used for classification through a linear layer.

Although the original ViTAE performs well on ImageNet classification, it is unsuitable for transferring to other tasks like segmentation, detection, pose estimation and so on, since it cannot generate abundant intermediate features at different scales. Thus, the authors propose the ViTAEv2 variant [28], which adopts the classic stage-wise design of popular backbone networks such as ResNet and Swin. Figure 2 shows the comparison between the original ViTAE and ViTAEv2. In ViTAEv2, the network is split into multiple stages, usually the number is 4. In each stage, the first cell is a reduction cell for downsampling, which is followed by the stacked normal cells. An average pooling layer is used after the last normal cell to replace the class tokens. When finetuning on downstream tasks, this pooling layer is removed and the remained network is connected with corresponding task decoders.

The reduction cell and normal cell are the two most important modules in ViTAE, they are constructed based on the typical transformer block. The reduction cell is used to serve for downsampling and provide multiscale context. Specifically, before fed into the normalization and MHSA layers, the features pass a pyramid reduction module (PRM) that incorporates multiple parallel convolutions with different dilation rates, where the strides control the ratio of spatial sampling. After PRM, the features from parallel branches are concatenated in the channel dimension. The PRM brings the scale-invariance inductive bias of CNN into ViTAE, while the locality modeling is finished by inputting the input features of PRM into a parallel convolutional module (PCM). The PCM is located in an additional branch paralleling to the global dependency path that includes PRM and MHSA, and it is made up of three successive convolutional layers. The first two layers are composed of the combination of Conv-BN-SiLU [57], while the last layer is constructed without BN operation [58]. The downsampling ratio of the PCM is same as the PRM by adjusting strides. The normal cell has a few changes compared with the reduction cell. Concretely, it dose not include the PRM. Thus, the resolution of its internal features is always the same. In addition, the features from MHSA, PCM and the original residual branch are combined together through element-wise addition before inputting into the feed forward network (FFN), while the same place in reduction cell has only two (without skip connection) because the PRM changes channel dimension. Since the MHSA and FFN process 1-D token sequence, while PRM and PCM process 2-D feature maps, Img2Seq and Seq2Img operations are used to reshape the features accordingly. In addition, the authors adopt group convolutions in PCM for saving parameters.

In this paper, we employ the ViTAEv2 model for RSP.

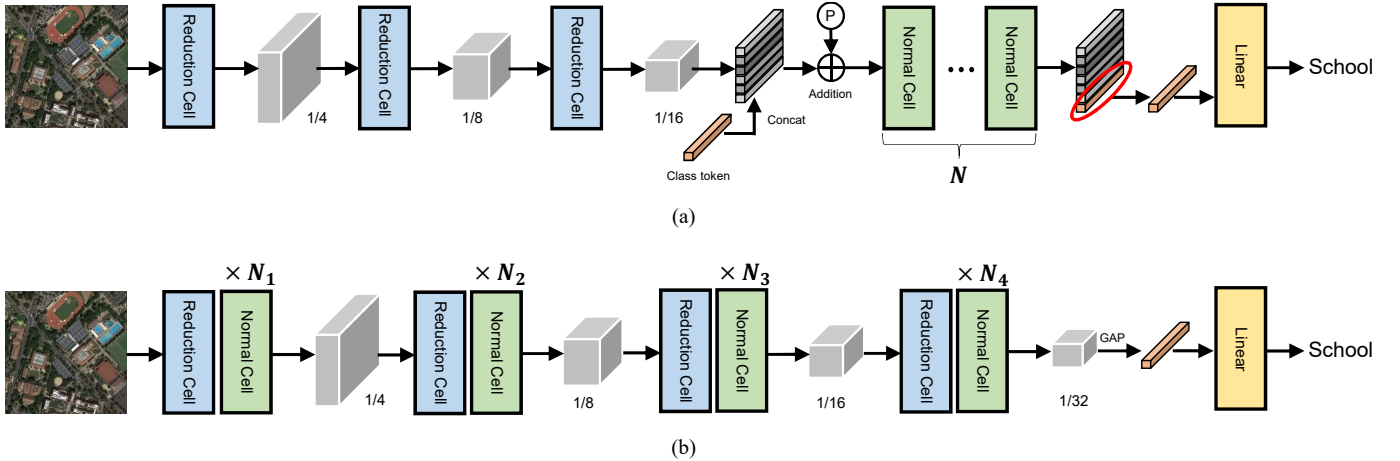


Fig. 2. The diagram of the adopted ViTAE models. (a) Original ViTAE [14]. (b) ViTAEv2 [28].

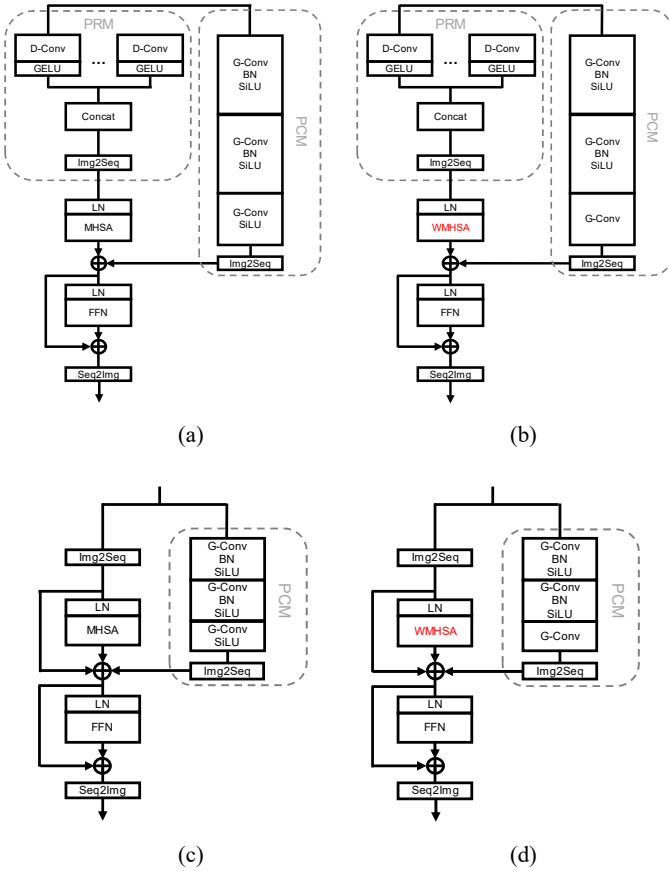


Fig. 3. The detailed structures of different cells in ViTAE models. (a) and (c) are the reduction cell and normal cell in the original ViTAE, while (b) and (d) are the corresponded variants in the ViTAEv2.

Concretely, inspired by Swin [13], some MHSAs in above cells are both replaced by the WMHSA to reduce the computational cost. Specifically, considering the feature size becomes smaller in the later stages, it is unnecessary to partition the feature for WMHSA. Thus, only the MHSAs in the first two stages are substituted by WMHSA. It should be noticed that the adopted WMHSA does not need to be shifted as the original implementation, since the WMHSA is conducted on the

TABLE I
THE HYPER PARAMETER SETTINGS OF DIFFERENT “SMALL” VERSION ViTAE MODELS. “P” DENOTES PERFORMER ATTENTION [56] WHILE “L” MEANS THE REDUCTION CELL HAS NO PCM AND ATTENTION. “F” DENOTES THE ORIGINAL MHSA WHILE “W” DENOTES THE WMHSA.

| Network | ViTAE-S [14] | ViTAEv2-S [28] |
|--------------------|--------------------------------|---|
| Stage | 3 | 4 |
| Downsampling Ratio | [4, 2, 2] | [4, 2, 2, 2] |
| Embedding Dim | [64, 64, 192] | [64, 64, 128, 256] |
| Stage Dim | [96, 192, 384] | [64, 128, 256, 512] |
| RC | Head Group Type | [1, 1, 1] [1, 1, 1] [P, P, L] |
| NC | Head Group Type Depth | [1, 1, 6] [1, 1, 96] [F, F, F] [0, 0, 14] |
| | | [1, 1, 2, 4] [1, 16, 32, 64] [W, W, F, F] [1, 2, 4, 8] [1, 32, 64, 128] [W, W, F, F] [2, 2, 8, 2] |

merged multiscale feature from PRM, where different regions have communicated with each other through the overlapped receptive fields of the sliding dilated convolutions. Besides, it is also not necessary to use relative positional encoding since the convolutions already encode the positional information. Additionally, the SiLU in the last convolutional layer of PCM is also removed to reduce nonlinearity. The detailed structures and comparisons of different cells in the original ViTAE and ViTAEv2 are shown in Figure 3.

In our implementation, we mainly evaluate the “small” version of the original ViTAE, named ViTAE-S. In addition, we also adopt the ViTAEv2-S model due to its excellent representation ability and transferability to downstream tasks. Table I lists the details of ViTAE-S and ViTAEv2-S. Here, the length of the corresponded list equals to the number of stages. “Embedding Dim” means the encoding dimension in PRM, while “Stage Dim” is the channel number of the feature through corresponding stage, which is useful for aligning the related downstream task decoders. The “RC” and “NC” separately represent the reduction cell and normal cell, where “Head” is the head number in MHSAs or WMHSAs, “Group” represents the number of group convolutions in PCM, and “Type” is the specific attention types. The ViTAE-S adopts

TABLE II
RESULTS OF DIFFERENT MODELS ON THE MINI-EVALUATION SET. THEY ARE TRAINED ON THE MINI-TRAINING SET FROM MILLIONAID.

| Model | Acc@1 | Acc@5 | Param(M) | Training Time (hh:mm:ss) |
|----------------|-------|-------|----------|--------------------------|
| ResNet-50 [12] | 80.8 | 96.1 | 23.6 | 16:42:58 |
| DeiT-S [37] | 72.9 | 92.9 | 21.7 | 16:57:39 |
| ViT-B [36] | 78.4 | 92.1 | 114.4 | 17:41:03 |
| PVT-S [38] | 80.0 | 94.1 | 23.9 | 18:06:42 |
| Swin-T [13] | 84.7 | 93.7 | 27.6 | 17:49:06 |
| ViTAE-S [14] | 85.9 | 96.9 | 22.8 | 24:00:35 |
| ViTAEv2-S [28] | 88.2 | 96.1 | 18.8 | 23:57:30 |

the performer of T2T-ViT [56] in the first two reduction cells. “L” means this reduction cell does not use PCM and attention. “F” and “W” separately denote the MHSA and WMHSA in ViT and Swin. At last, the “Depth” is the number of stacked normal cells, which is also the N_i in Figure 2.

C. Implementation

1) *Determine the Pretraining Network:* We first determine the type of deep models to be used for RSP. To this end, we construct a mini-training set and mini-evaluation set from the official training set, which have 9,775 and 225 images, respectively. Note the latter set is formed by randomly selecting 5 images from each category to balance the classes. For CNN, the classic ResNet-50 [12] is employed. Since this research mainly explores the performance of vision transformer models with RSP, a series of typical vision transformer based networks including DeiT-S [37], PVT-S [38], and Swin-T [13], are also evaluated. The selection of specific version is to guarantee these models have similar amount of parameters compared with the ViTAE-S model. In addition, we also include ViT-B [36] for reference since ViT is the most basic model of vision transformers.

All models are trained 300 epochs with batchsize 16. We adopt the AdamW optimizer where the momentum is set to 0.9 and the weight decay is set to 0.05. The initial learning rate is 1e-3, which is adjusted by the cosine scheduling policy: $current_lr = min_lr + \frac{1}{2}(initial_lr - min_lr)(1 + \cos(\frac{iter}{max_iter}\pi))$, where min_lr is 5e-6. In addition, we set the warming up epochs to 5, where the learning rate is set to 5e-7. Following the typical IMP, the input image is resized to 224×224 by randomly cropping during training, while during testing, the image at the same size is obtained through “center crop”. In addition, a series of data augmentations including AutoAugment [59], Random Erasing [60], Mixup [61], CutMix [62], and color jitter are applied to improve the training performance. The top-1 accuracy and top-5 accuracy are used as the evaluation metrics. In addition, all models are implemented on a single NVIDIA Tesla V100 GPU, and the results are shown in Table II.

It can be seen that despite the ViT-B has the most parameters, it performs not well than the classic ResNet-50. The DeiT-S performs the worst since we do not adopt the teacher model. Because our task is pretraining using remote sensing images, obtaining the corresponding teacher model is our target instead of prerequisite. By introducing the design paradigm of feature pyramid, PVT-S improves the accuracy compared with ViT-B. On this foundation, the original ViTAE-S further considers

TABLE III
RESULTS OF ViTAEV2-S WITH DIFFERENT SETTINGS OF TRAINING EPOCH ON THE MILLIONAID VALIDATION SET.

| Epoch | Acc@1 | Acc@5 |
|-------|-------|-------|
| 5 | 94.53 | 99.41 |
| 10 | 96.45 | 99.64 |
| 15 | 97.38 | 99.74 |
| 20 | 98.00 | 99.81 |
| 40 | 98.64 | 99.86 |
| 60 | 98.87 | 99.83 |
| 80 | 98.90 | 99.85 |
| 100 | 98.97 | 99.88 |

the locality and scale-invariance modelling, which are the inductive biases of conventional CNN models. However, it cost much training time since the token number in the early RCs is large, requiring more computations. The Swin-T addresses this issue by restricting the MHSA in fixed windows, and adopts the image shifting to implicitly promote the communications between windows. By taking the advantage of WMHSA, the ViTAEv2-S achieves the best performance and it exceeds the second place by 2.3% top-1 accuracy.

The procedure of model determination is shown as follows. For the ViTAE models, we choose the strongest one to expect good performance in downstream tasks such as the aerial scene recognition when adopting RSP, i.e., the ViTAEv2-S. For comparison, the ResNet-50 is selected as the representative network in conventional CNN, and the remote sensing pretrained ResNet-50 can also provide a group of new CNN related baselines on a series of aerial dataset. The DeiT-S and ViT-B are eliminated because of the low accuracy and large number of parameters, and they are difficult to be transferred into downstream tasks because of the design of stacking transformers. The Swin can be regarded as building on the foundation of PVT by substituting the global MHSA to the shiftable WMHSA. Since the top-1 accuracy of Swin is larger than PVT, and Swin-T requires less training time, we also choose Swin-T in the subsequent experiments.

2) *Obtain the Suitable Weights:* After determining the model candidates, we conduct the RSP to obtain the pretrained weights. Concretely, maintaining the category balance, we randomly choose 1,000 images in each category of the Million-AID dataset to form the validation set that has 51,000 images, achieving a similar volume compared with the ImageNet validation set, which contains 50,000 images. The remained 949,848 images are used for training. Although the number of images and number of categories for RSP are less than those of the ImageNet training set, it still can perform to be competitive or even achieves SOTA results on aerial scene tasks, whose details will be presented later.

TABLE IV

RESULTS OF THE CANDIDATE MODELS FOR THE SUBSEQUENT FINETUNING EXPERIMENTS ON THE MILLIONAID VALIDATION SET.

| Epoch | Acc@1 | Acc@5 |
|------------------|-------|-------|
| ResNet-50 | | |
| 40 | 97.99 | 99.81 |
| 120 | 98.76 | 99.83 |
| 300 | 98.99 | 99.82 |
| Swin-T | | |
| 40 | 97.80 | 99.84 |
| 120 | 98.63 | 99.89 |
| 300 | 98.59 | 99.88 |
| ViTAEv2-S | | |
| 40 | 98.64 | 99.86 |
| 100 | 98.97 | 99.88 |

To obtain suitable pretraining weights, we separately train the ViTAEv2-S model under the configuration of different epochs. The basic learning rate is 5e-4, and the batchsize is set to 384. The remained settings are same with the previous experiment. All experiments are conducted with 4 V100 GPUs, and the results are shown in Table III. According to the results, it can be observed that the model start saturation after about 40 epochs, since it only improves 0.64% top-1 accuracy compared with training 20 epochs, while the next 20 epochs only brings a gain of 0.23%. Thus, the network weights trained with 40 epochs are firstly chosen as the RSP parameters of ViTAEv2-S to be applied into the subsequent tasks. Intuitively, the model achieving good performance on the large-scale pretraining dataset will also perform well on the downstream tasks. Therefore, we also use the the network weights trained with 100 epochs in the downstream tasks. These models are separately denoted with the suffix “E40” and “E100”.

For ResNet-50 and Swin-T, we follow [13] to configure the training settings, where the networks are trained for 300 epochs. In the experiments, we observe that the top-1 accuracy of Swin-T-E120 on validation set is roughly equivalent to ViTAEv2-S-E40. Thus, the training weights of Swin-T-E120 are selected. Similarly, we also choose the final network weights Swin-T-E300 as a comparion with ViTAEv2-S-E100. To make the experiments fair, the weights of ResNet-50 and Swin-T that trained with 40 epochs are also considered, since they are trained using the same number of epochs with the ViTAEv2-S-E40.

The final pretraining models are listed in Table IV. It can be seen that the validation accuracies are almost increasing with the increase of training epochs. However, the performance of Swin-T-E300 is not as well as Swin-T-E120. Nonetheless, we still keep it since it may have stronger generalization by seeing more diverse samples.

IV. FINETUNING ON DOWNSTREAM TASKS

In this section, the pretrained models are further finetuned on a series of downstream tasks, including the scene recognition, semantic segmentation, object detection in aerial scenes as well as the change detection. It should be clarified that models for the scene recognition in this section are trained and evaluated on commonly used aerial scene dataset rather than the MillionAID engaging for RSP.

A. Aerial Scene Recognition

We first introduce the used scene recognition datasets and the implementation details, then present the the experimental results and analyses.

1) *Dataset*: The three most popular scene recognition datasets including the UC Merced Land Use (UCM) dataset [63], the Aerial Image Dataset (AID) [64] and the benchmark for REmote Sensing Image Scene Classification that is created by Northwestern Polytechnical University (NWPU-RESISC) [21], are used to comprehensively evaluate the impact of RSP and the representation ability of the above adopted backbones.

- UCM: This the most important dataset for scene recognition. It contains 2,100 images whose sizes are all 256 × 256 and have the pixel resolution of 0.3m. The 2,100 images equally belong to 21 categories. Thus, each category has 100 images. All samples are manually extracted from the large images that in the USGS National Map Urban Area Imagery Database collected from various urban areas around the country.
- AID: This is a challenging dataset, which is generated by collecting the images from multi-source sensors on GE. It has high intra-class diversities since the images are carefully chosen from different countries. And they are extracted at different time and seasons under different imaging conditions. It totally has 10,000 images at the size of 600 × 600, belonging to 30 categories.
- NWPU-RESISC: This dataset is characterized by a great number of samples. It contains 31,500 images and 45 categories in total, where each category has 700 samples. Each image has 256 × 256 pixels. The spatial resolutions are varied from 0.2m to 30m. Some special landforms, such as islands, lakes, regular mountains, and snow mountains, may be in lower resolutions.

2) *Implementation Detail and Experimental Setting*: The training settings are same with previous experiments. The training epoch and batchsize are set to 200 and 64, respectively. These experiments are conducted on a single V100 GPU. Following [33], five settings of these three datasets are adopted to comprehensively evaluate the remote sensing pre-trained models and make the experiments become convincible, including UCM (8:2), AID (2:8), AID (5:5), NWPU-RESISC (1:9), and NWPU-RESISC (2:8). Note the $m : n$ means $10m\%$ samples are used for training, while the others form the testing set. Similar with previous section, the images in each category are proportionally divided into two groups that are separately used for training and evaluation, respectively. Besides the above three backbones we selected, the ImageNet pretrained ResNet-50 and the ResNet-50 pretrained by SeCo [50] – a remote sensing self-supervised method considering seasonal variation, are also adopted for a fair comparison. When implementing finetuning on each scene recognition task, only the neuron number of the last linear layer is changed to match the categories of the target dataset. The overall accuracy (OA), which is the most commonly used criterion in aerial scene recognition community by counting the proportion of the correct classified images relative to all images in the testing set, is utilized in the experiments. The models are repeatedly

TABLE V

RESULTS OF THE SELECTED MODELS AND SOTA METHODS ON THE THREE SCENE RECOGNITION DATASETS UNDER DIFFERENT SETTINGS. THE BOLD FONTS IN THE LAST THREE GROUPS MEAN THE BEST RESULTS, WHILE “*” DENOTES THE BEST AMONG ALL MODELS.

| Model | Publication | UCM (8:2) | AID (2:8) | AID (5:5) | NWPU-RESISC (1:9) | NWPU-RESISC (2:8) |
|--|-------------|----------------------|----------------------|---------------------|----------------------|----------------------|
| CBAM [34] | ECCV2018 | 99.04 ± 0.23 | 94.66 ± 0.39 | 96.90 ± 0.04 | 92.10 ± 0.04 | 94.26 ± 0.12 |
| EAM (IMP-ResNet-50) [65] | GRSL2021 | 98.98 ± 0.37 | 93.64 ± 0.25 | 96.62 ± 0.13 | 90.87 ± 0.15 | 93.51 ± 0.12 |
| F ² BRBM (IMP-ResNet-50) [66] | JSTARS2021 | 99.58 ± 0.23 | 96.05 ± 0.31 | 96.97 ± 0.22 | 92.74 ± 0.23 | 94.87 ± 0.15 |
| MBLANet (IMP-ResNet-50) [33] | TIP2021 | 99.64 ± 0.12 | 95.60 ± 0.17 | 97.14 ± 0.13 | 92.32 ± 0.15 | 94.66 ± 0.11 |
| GRMANet (IMP-ResNet-50) [67] | TGRS2021 | 99.19 ± 0.10 | 95.43 ± 0.32 | 97.39 ± 0.24 | 93.19 ± 0.42 | 94.72 ± 0.25 |
| IDCCP (IMP-ResNet-50) [68] | TGRS2021 | 99.05 ± 0.20 | 94.80 ± 0.18 | 96.95 ± 0.13 | 91.55 ± 0.16 | 93.76 ± 0.12 |
| ESD-MBENet-v1 (IMP-ResNet-50) [25] | TGRS2021 | 99.81 ± 0.10 | 96.00 ± 0.15 | 98.54 ± 0.17 | 92.50 ± 0.22 | 95.58 ± 0.08 |
| ESD-MBENet-v2 (IMP-ResNet-50) [25] | TGRS2021 | 99.86 ± 0.12 | 95.81 ± 0.24 | 98.66 ± 0.20 | 93.03 ± 0.11 | 95.24 ± 0.23 |
| ARCNet (IMP-VGG-16) [69] | TGRS2019 | 99.12 ± 0.40 | 88.75 ± 0.40 | 93.10 ± 0.55 | — | — |
| SCCov (IMP-VGG-16) [70] | TNNLS2019 | 99.05 ± 0.25 | 93.12 ± 0.25 | 96.10 ± 0.16 | 89.30 ± 0.35 | 92.10 ± 0.25 |
| KFBNNet (IMP-DenseNet-121) [71] | TGRS2020 | 99.88 ± 0.12 | 95.50 ± 0.27 | 97.40 ± 0.10 | 93.08 ± 0.14 | 95.11 ± 0.10 |
| GBNet (IMP-VGG-16) [24] | TGRS2020 | 98.57 ± 0.48 | 92.20 ± 0.23 | 95.48 ± 0.12 | — | — |
| MG-CAP (IMP-VGG-16) [72] | TIP2020 | 99.00 ± 0.10 | 93.34 ± 0.18 | 96.12 ± 0.12 | 90.83 ± 0.12 | 92.95 ± 0.13 |
| EAM (IMP-ResNet-101) [65] | GRSL2021 | 99.21 ± 0.26 | 94.26 ± 0.11 | 97.06 ± 0.19 | 91.91 ± 0.22 | 94.29 ± 0.09 |
| IMP-ViT-B [36] | ICLR2021 | 99.28 ± 0.23 | 93.81 ± 0.21 | 96.08 ± 0.14 | 90.96 ± 0.08 | 93.96 ± 0.17 |
| MSANet (IMP-ResNet-101) [73] | JSTARS2021 | 98.96 ± 0.21 | 93.53 ± 0.21 | 96.01 ± 0.43 | 90.38 ± 0.17 | 93.52 ± 0.21 |
| CTNet (IMP-MobileNet-V2+IMP-ViT-B) [44] | GRSL2021 | — | 96.25 ± 0.10 | 97.70 ± 0.11 | 93.90 ± 0.14 | 95.40 ± 0.15 |
| LSENet (IMP-VGG-16) [31] | TIP2021 | 99.78 ± 0.18 | 94.41 ± 0.16 | 96.36 ± 0.19 | 92.23 ± 0.14 | 93.34 ± 0.15 |
| DFAGCN (IMP-VGG-16) [23] | TNNLS2021 | 98.48 ± 0.42 | — | 94.88 ± 0.22 | — | 89.29 ± 0.28 |
| MGML-FENet (IMP-DenseNet-121) [26] | TNNLS2021 | 99.86 ± 0.12 | 96.45 ± 0.18 | 98.60 ± 0.04 | 92.91 ± 0.22 | 95.39 ± 0.08 |
| ESD-MBENet-v1 (IMP-DenseNet-121) [25] | TGRS2021 | 99.86 ± 0.12 | 96.20 ± 0.15 | 98.85 ± 0.13* | 93.24 ± 0.15 | 95.50 ± 0.09 |
| ESD-MBENet-v2 (IMP-DenseNet-121) [25] | TGRS2021 | 99.81 ± 0.10 | 96.39 ± 0.21 | 98.40 ± 0.23 | 93.05 ± 0.18 | 95.36 ± 0.14 |
| IMP-ResNet-50 [12] | CVPR2016 | 98.81 ± 0.23 | 94.67 ± 0.15 | 95.74 ± 0.10 | 90.09 ± 0.13 | 94.10 ± 0.15 |
| SeCo-ResNet-50 [50] | ICCV2021 | 97.86 ± 0.23 | 93.47 ± 0.08 | 95.99 ± 0.13 | 89.64 ± 0.17 | 92.91 ± 0.13 |
| RSP-ResNet-50-E40 | Ours | 99.43 ± 0.24 | 95.88 ± 0.07 | 97.29 ± 0.07 | 92.86 ± 0.09 | 94.40 ± 0.05 |
| RSP-ResNet-50-E120 | Ours | 99.52 ± 0.15 | 96.60 ± 0.04 | 97.78 ± 0.08 | 93.76 ± 0.03 | 94.97 ± 0.07 |
| RSP-ResNet-50-E300 | Ours | 99.48 ± 0.10 | 96.81 ± 0.03 | 97.89 ± 0.08 | 93.93 ± 0.10 | 95.02 ± 0.06 |
| IMP-Swin-T [13] | ICCV2021 | 99.62 ± 0.19 | 96.55 ± 0.03 | 98.10 ± 0.06 | 92.73 ± 0.09 | 94.70 ± 0.10 |
| RSP-Swin-T-E40 | Ours | 99.24 ± 0.18 | 95.95 ± 0.06 | 97.52 ± 0.04 | 91.22 ± 0.18 | 93.30 ± 0.08 |
| RSP-Swin-T-E120 | Ours | 99.52 ± 0.00 | 96.73 ± 0.07 | 98.20 ± 0.02 | 92.02 ± 0.14 | 93.84 ± 0.07 |
| RSP-Swin-T-E300 | Ours | 99.52 ± 0.00 | 96.83 ± 0.08 | 98.30 ± 0.04 | 93.02 ± 0.12 | 94.51 ± 0.05 |
| IMP-ViTAEv2-S [28] | arXiv2022 | 99.71 ± 0.10 | 96.61 ± 0.07 | 98.08 ± 0.03 | 93.90 ± 0.07 | 95.29 ± 0.12 |
| RSP-ViTAEv2-S-E40 | Ours | 99.71 ± 0.10 | 96.72 ± 0.06 | 97.92 ± 0.06 | 94.12 ± 0.07 | 95.35 ± 0.03 |
| RSP-ViTAEv2-S-E100 | Ours | 99.90 ± 0.13* | 96.91 ± 0.06* | 98.22 ± 0.09 | 94.41 ± 0.11* | 95.60 ± 0.06* |

trained and evaluated with five times at each setting, and the average value μ and standard deviation σ of the results in different trials are recorded as $\mu \pm \sigma$.

3) Experimental Results: Quantitative Results and Analyses: Table V presents the results of the above selected backbones pretrained using different methods and other SOTA methods. Since this research only focus on pretraining of deep networks, especially the vision transformers. We only lists the deep learning based aerial scene recognition methods. For convenience, the “IMP” and “RSP” are used to represent “ImageNet Pretraining” and “Remote Sensing Pretraining”, respectively. It can be seen that the methods are split into five groups. The first group is the methods that adopt ResNet-50 as the backbone network, where the ResNet-50 is initialized by the ImageNet pretrained weights. This group can be used to compare with the third group. The second group includes the recent existing advanced methods whose backbone is other popular networks except for ResNet-50, such as the ImageNet pretrained VGG-16, ResNet-101, DenseNet-121 and so on. Then, the ResNet-50, Swin-T and ViTAEv2-S networks, whose pretrained weights are obtained by IMP, RSP or SeCo, form the last three groups, respectively. In addition, it should be noted that besides the network types, the weights pretrained for different epochs are also considered. The bold fonts in the last three groups mean the best results in each group, while “*” denotes the best among all models (same meanings in other tasks).

On the foundation of ImageNet pretrained ResNet-50, many methods are developed, which have been shown in the first

group. Among these methods, many flexible and advanced modules have been explored. For example, the attention mechanisms (CBAM [34], EAM [65], MBLANet [33]), where specific channels or spatial positions of the features are highlighted, and multiscale features (F²BRBM [66] and GRMANet [67]), where the intermediate features are also employed. In addition, the self-distillation technology combined with specially designed loss functions (ESD-MBENet [25]) and the multibranch siamese networks (IDCCP [68]) have also been applied. While in the second group, the more diverse frameworks with various backbones are presented. Besides the traditional CNN, the recent ViT has also been applied in some works. Compared with the IMP-ViT-B, the RSP-Swin-T-E300 performs better, although the former model has more trainable parameters. It can be observed that the backbones are changing over time. The VGG-16 used in early years is gradually replaced by the deeper networks such as ResNet-101 or DenseNet-121 due to their better representation ability.

In the implemented networks, the SeCo-ResNet-50 performs the worst compared with its counterparts, it is mainly due the fact that there still exist a gap between the Sentinel-2 multispectral images where the SeCo trained on with the RGB images for aerial scenes recognition. Compared with the ImageNet pretrained ResNet-50, our remote sensing pretrained ResNet-50 improves the accuracy on all settings. These results imply that RSP brings a better starting point for the optimization of the subsequent finetuning process, attributing to the aerial images used for pretraining compared with the natural images in ImageNet. Similarly, the RSP-Swin-T outperforms IMP-

Swin-T on three settings and achieves comparable results on the other two settings. In addition, the ResNet-50 and Swin-T can perform to be competitive compared other complicated methods by only using the RSP weights without changing the network structures. Besides, when comparing the ImageNet pretrained ResNet-50 and Swin-T, we can find that the IMP-Swin-T performs better on all settings, since the vision transformers have stronger context modeling capability. While being initialized by RSP weights, the ResNet becomes to be more competitive and surpasses the IMP-Swin-T on the AID (2:8), NWPU-RESISC (1:9), and NWPU-RESISC (2:8) settings, showing the benefit of RSP again. Owing to excellent representation ability of ViTAEv2-S, which has both the locality modelling ability and long-range dependency modelling ability, it outperforms both ResNet-50 and Swin-T on almost all the settings, regardless of IMP and RSP. Moreover, the RSP-ViTAEv2-S achieves the best performance compared with all other methods on almost all settings except for the AID (5:5), though on which it also delivers comparable performance with the best one, i.e., RSP-Swin-T-E300.

In our experiments, it can be observed that the remote sensing pretrained models converge faster and obtain better performance on small datasets, proving our intuition that the remote sensing pretrained weights are easier to transfer between aerial scenes. While for the case where training samples are abundant, like AID (5:5), the representation ability of deeper models can be fully exploited. For example, the DenseNet-121 based ESD-MBENeT obtain the best accuracy. Nevertheless, it should be noted that only the feature output from the last layer of RSP-ResNet-50, RSP-Swin-T or RSP-ViTAEv2-S is used for classification, and it is expected that their performance can be further improved when employing the multilayer intermediate features. In this sense, these remote sensing pretrained models can serve as effective backbones for future research in the aerial recognition field. Furthermore, Table V also shows that the models pretraining with more epochs will probably have stronger representation abilities. Since RSP-ResNet-50-E40 and RSP-Swin-T-E40 fall behind their counterparts with more epochs, we only evaluate the “E120” and “E300” pretrained weights for these two types of networks in the rest experiments, while for ViTAEv2-S, both the “E40” and “E100” weights are still used.

Qualitative Results and Analyses: Figure 4 shows the response maps of the above evaluated models using Grad-CAM++ [74] on images from various scenes. The warmer the color is, the higher the response is. To better show the impact of RSP, we use the pretrained weights of “E300” for ResNet-50 and Swin-T, and the weights of “E100” for ViTAEv2-S. The first three rows are the natural landscapes, and the scenes in 4-8 rows mainly contain specific foreground objects, while the next six rows present some scenes with different artificial constructions. For example, the “Thermal power station” scene includes not only chimneys, but also cooling towers.

Corresponding to the quantitative results in Table V, the response maps of SeCo-ResNet-50 are scattered and it can not precisely capture the semantic-relevant areas, especially on the natural landscapes or complex scenes with artificial constructions. Compared with the IMP-ResNet-50, the RSP-

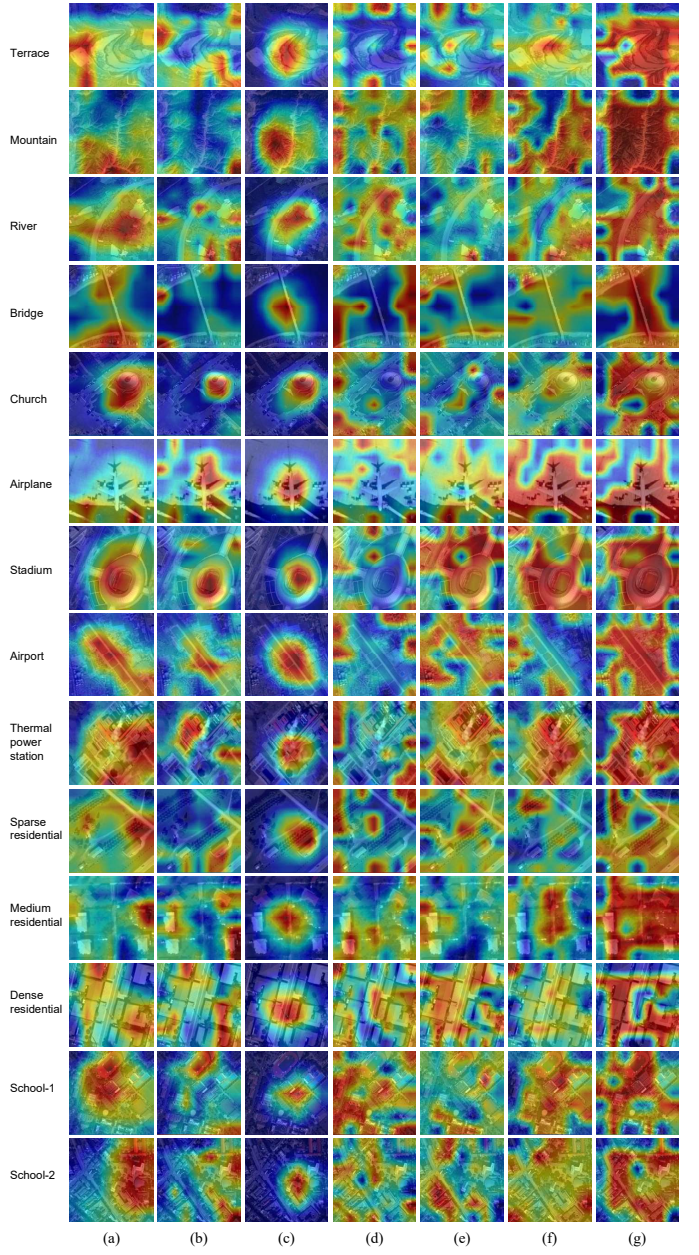


Fig. 4. Response maps of the evaluated models on different scenes. (a) IMP-ResNet-50. (b) SeCo-ResNet-50. (c) RSP-ResNet-50. (d) IMP-Swin-T. (e) RSP-Swin-T. (f) IMP-ViTAEv2-S. (g) RSP-ViTAEv2-S.

ResNet-50 pays more attention to the important targets. It implies that RSP facilitates ResNet-50 to learn better semantic representations, probably by seeing semantic-similar images in the MillionAID dataset. Compared to the ResNet-50, the Swin-T has a better context modelling ability by attending far away regions with the help of MHSAs. Thus, their range of high response areas are wider. Surprisingly, the IMP-Swin-T mainly concentrates on background context, but the foreground responses have been enhanced when adopting the RSP. By combining the advantages of CNN and vision transformers, the ViTAEv2-S achieves a comprehensive perception of the whole scene. Especially, the RSP-ViTAEv2-S can better recognize the typical natural remote sensing scenes, such as

terrace, mountain and river. On the foreground object based scenes, compared with RSP-ResNet-50, the RSP-ViTAEv2-S not only focus on the primary objects, it also considers the related regions in background. While on the objects, the RSP-ViTAEv2-S assigns higher attentions, such as the airplane with a warmer color compared with IMP-ViTAEv2-S. On the residential areas that with complex object distributions, the RSP-ViTAEv2-S has the ability of correctly capturing the sparse buildings and connecting these regions to form a holistic representation, effectively perceive the overall information of the scene. On the first image of school scene, the RSP-ViTAEv2-S simultaneously focuses on the playground and the surroundings, surpassing the SeCo-ResNet-50. As for the “school-2” image that is even difficult to be recognized by human, these models show different recognition priorities. For example, the RSP-ViTAEv2-S not only considers the campus (it can be possibly distinguished by the irregular shape of buildings) like the IMP-ReNet-50, but also notices the around roads. The results in Table V and Figure 4 validate the effectiveness of RSP and the superiority of vision transformers in the aerial scene recognition task.

B. Aerial Semantic Segmentation

Aerial semantic segmentation is also a classification task like aerial scene recognition but at the pixel level rather than the scene level. We then evaluate the above three models on the aerial semantic segmentation task, including the scene parsing and object segmentation subtasks, where the former focuses on labeling each pixel of the whole scene, while the latter emphasizes the segmentation of foreground objects.

1) *Dataset*: We use the ISPRS Potsdam dataset¹ and the large-scale segmentation benchmark — iSAID [75], to serve as the test bed of the corresponded subtasks, respectively.

- **Potsdam**: This dataset is released by ISPRS Commission WG II/4. It covers a large scene that is collected over 3.42 km^2 area of the Potsdam city. It contains 38 images, whose average size is $6,000 \times 6,000$ pixels, and the resolution is 0.5m. Among them, the training and testing set separately have 24 and 14 images. There are 6 categories included in these scenes, namely impervious surfaces, building, low vegetation, tree, car, and clutter.

- **iSAID**: This a large-scale dataset that mainly for instance segmentation. Also, it provides the semantic mask including 15 foreground and 1 background categories over the aerial objects. It consists of 2,806 high resolution images that range from 800×800 to $4,000 \times 13,000$ pixels. The training, validation and test set separately have 1,411, 458 and 937 images. In this paper, only the validation set is used for evaluation since the testing set is unavailable.

2) *Implementation Detail and Experimental Setting*: We adopt different settings for the above backbone networks by following the common practice. Concretely, the ResNet based networks are trained with the mini-batch stochastic gradient descent with momentum (SGDM) strategy, where the initial learning rate, weight decay and momentum are separately set

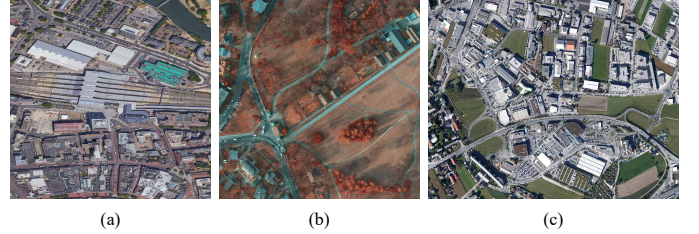


Fig. 5. Visual samples from different datasets: (a) MillionAID, (b) Potsdam, and (c) iSAID.

to 0.01, 0.0005 and 0.9. The learning rate is optimized by the polynomial scheduler: $\text{current_lr} = \text{min_lr} + \text{initial_lr} \cdot (1 - \frac{\text{iter}}{\text{max_iter}})^{\text{power}}$, where $\text{min_lr} = 0.0001$, $\text{power} = 0.9$. While for the vision transformers, such as the Swin-T and ViTAEv2-S, they are trained using the AdamW optimizer, whose learning rate and weight decay are 6e-5 and 0.01. The learning rate schedule adopts the polynomial decay policy with a power of 1.0 and min_lr of 0. They also have a linear warming up stage at the first 1,500 iterations with the initial learning rate of 1e-6. For a fair comparison, all networks are training 80k iterations with a batchsize of 8. Following [13], [14], we use the UperNet [15] as the unified segmentation framework for all the pretrained backbones, since the output stride equals to 32. All methods are implemented based on mmsegmentation [76]. For the convenience of training, the Potsdam and iSAID are separately sampled and cropped into patches with a size of 512×512 and 896×896 with a stride of 384 and 512, respectively. We use the random horizontal flipping data augmentation strategy. Following the evaluation protocol in the aerial segmentation community, for Potsdam dataset, we report the OA, mean F1 score (mF1) and per class F1 score. Note that the clutter category is regarded as the background and ignored during computing loss and evaluation metrics. While for iSAID dataset, the intersection over union (IoU) of foreground categories and the average IOU of all classes (including background) are calculated. All evaluations are conducted in a single scale for a fair comparison.

3) *Experimental Results: Quantitative Results and Analyses*: Table VI-VII present the segmentation results of our methods and other SOTA methods. It can be seen that, when changing the backbone from ResNet-50 to Swin-T, and then to ViTAEv2-S, the performance is increased. The results are consistent to the aforementioned scene recognition results, showing the better representation ability of vision transformers. Although the ViTAEv2-S obtains the highest OA on the Potsdam dataset, its mF1 is not as well as LANet [86]. From Table VII, we can find that the score of the “Car” category of the selected models are worse than other methods. We suspect that it may be because of the encoder-decoder structure and the rough feature fusion strategy in the UperNet, where the high resolution features have not encoded sufficient high-level semantics, while LANet [86] not only simultaneously enhance the high- and low-level features, it also enriches the semantics of the high resolution features. Thus, the segmentation performance of the evaluated models based on UperNet on the small objects, such as cars, need to

¹<https://www.isprs.org/education/benchmarks/UrbanSemLab/2d-sem-label-potsdam.aspx>

TABLE VI
RESULTS OF THE UPERNET SEGMENTATION MODEL WITH DIFFERENT BACKBONES AND SOTA METHODS ON THE TESTING SET OF POTS DAM DATASET.

| Method | Backbone | OA | mF1 | F1 score per category | | | | |
|-----------------------|----------------|---------------|--------------|-----------------------|--------------|--------------|--------------|--------------|
| | | | | Imper. surf. | Building | Low veg. | Tree | Car |
| FCN [77] | IMP-VGG-16 | 85.59 | 87.61 | 88.61 | 93.29 | 83.29 | 79.83 | 93.02 |
| S-RA-FCN [78] | IMP-VGG-16 | 88.59 | 90.17 | 91.33 | 94.70 | 86.81 | 83.47 | 94.52 |
| Multi-filter CNN [79] | IMP-VGG-16 | 90.65 | 85.23 | 90.94 | 96.98 | 76.32 | 73.37 | 88.55 |
| FCN [77] | IMP-ResNet-50 | 89.42 | 88.66 | 91.46 | 96.63 | 85.99 | 86.94 | 82.28 |
| DANet [80] | IMP-ResNet-50 | 89.72 | 89.14 | 91.61 | 96.44 | 86.11 | 88.04 | 83.54 |
| PSPNet [81] | IMP-ResNet-50 | 89.45 | 90.51 | 91.61 | 96.30 | 86.41 | 86.84 | 91.38 |
| DeeplabV3+ [82] | IMP-ResNet-50 | 89.74 | 90.94 | 92.35 | 96.77 | 85.22 | 86.79 | 93.58 |
| ResT [83] | IMP-ResNet-50 | 89.13 | 90.89 | 91.14 | 95.11 | 86.30 | 87.27 | 94.63 |
| EaNet [84] | IMP-ResNet-50 | 90.15 | 91.73 | 92.87 | 96.30 | 86.16 | 87.99 | 95.30* |
| BotNet [85] | IMP-ResNet-50 | 90.42 | 91.77 | 92.34 | 96.30 | 87.32* | 88.74* | 94.17 |
| LANet [86] | IMP-ResNet-50 | 90.84 | 91.95* | 93.05 | 97.19* | 87.30 | 88.04 | 94.19 |
| UperNet | IMP-ResNet-50 | 90.64 | 89.96 | 92.30 | 96.14 | 85.93 | 85.66 | 89.76 |
| UperNet | SeCo-ResNet-50 | 89.64 | 89.03 | 91.21 | 94.92 | 85.12 | 84.89 | 89.02 |
| UperNet | RSP-ResNet-50 | 90.61 | 89.94 | 92.42 | 96.15 | 85.75 | 85.49 | 89.87 |
| UperNet | IMP-Swin-T | 91.17 | 90.60 | 92.94 | 96.66 | 86.54 | 85.87 | 90.98 |
| UperNet | RSP-Swin-T | 90.78 | 90.03 | 92.65 | 96.35 | 86.02 | 85.39 | 89.75 |
| UperNet | IMP-ViTAEv2-S | 91.60* | 91.00 | 93.34* | 96.84 | 87.28 | 86.38 | 91.18 |
| UperNet | RSP-ViTAEv2-S | 91.21 | 90.64 | 93.05 | 96.62 | 86.62 | 85.89 | 91.01 |

TABLE VII
RESULTS OF THE UPERNET SEGMENTATION MODEL WITH DIFFERENT BACKBONES AND SOTA METHODS ON THE VALIDATION SET OF iSAID DATASET.

| Method | Backbone | mIOU | IOU per category ¹ | | | | | | | | | | | | | | |
|-------------------|------------------|--------------|-------------------------------|--------------|-------------|-------------|-------------|--------------|-------------|--------------|--------------|--------------|-------------|-------------|--------------|--------------|--------------|
| | | | Ship | ST | BD | TC | BC | GTF | Bridge | LV | SV | HC | SP | RA | SBF | | |
| FCN [77] | IMP-VGG-16 | 41.7 | 51.7 | 22.9 | 26.4 | 74.8 | 30.2 | 27.9 | 8.2 | 49.3 | 37.0 | 0 | 30.7 | 51.9 | 52.1 | | |
| UNet [87] | - | 39.2 | 49.0 | 0 | 36.5 | 78.6 | 22.9 | 5.5 | 7.5 | 49.9 | 35.6 | 0 | 38.0 | 46.5 | 9.7 | | |
| DenseASPP [88] | IMP-DenseNet-121 | 56.8 | 61.1 | 50.0 | 67.5 | 86.1 | 56.6 | 52.3 | 29.6 | 57.1 | 38.4 | 0 | 43.3 | 64.8 | 74.1 | | |
| DenseUNet [89] | IMP-DenseNet-121 | 58.7 | 66.1 | 50.4 | 76.1 | 86.2 | 57.7 | 49.5 | 33.9 | 54.7 | 46.2 | 0 | 45.1 | 65.9 | 71.9 | | |
| Semantic FPN [90] | IMP-ResNet-50 | 59.3 | 63.7 | 59.5 | 71.8 | 86.6 | 57.8 | 51.6 | 34.0 | 59.2 | 45.1 | 0 | 46.4 | 68.7 | 73.6 | | |
| RefineNet [91] | IMP-ResNet-50 | 60.2 | 63.8 | 58.6 | 72.3 | 85.3 | 61.1 | 52.8 | 32.6 | 58.2 | 42.4 | 23.0 | 43.4 | 65.6 | 74.4 | | |
| PSPNet [81] | IMP-ResNet-50 | 60.3 | 65.2 | 52.1 | 75.7 | 85.6 | 61.1 | 60.2 | 32.5 | 58.0 | 43.0 | 10.9 | 46.8 | 68.6 | 71.9 | | |
| DeeplabV3 [92] | IMP-ResNet-50 | 59.0 | 59.7 | 50.5 | 77.0 | 84.2 | 57.9 | 59.6 | 32.9 | 54.8 | 33.7 | 31.3 | 44.7 | 66.0 | 72.1 | | |
| DeeplabV3+ [82] | IMP-ResNet-50 | 60.8 | 63.9 | 52.5 | 72.8 | 84.9 | 56.5 | 58.9 | 32.2 | 59.1 | 42.9 | 31.4 | 46.1 | 67.7 | 72.9 | | |
| EMANet [93] | IMP-ResNet-50 | 55.4 | 63.1 | 68.4 | 66.2 | 82.7 | 56.0 | 18.8 | 42.1 | 58.2 | 41.0 | 33.4 | 38.9 | 46.9 | 78.5 | | |
| ASP-OCNet [94] | IMP-ResNet-50 | 40.2 | 47.3 | 40.2 | 44.4 | 65.0 | 24.1 | 29.9 | 27.1 | 46.3 | 13.6 | 10.3 | 34.6 | 37.9 | 41.4 | | |
| DANet [80] | IMP-ResNet-50 | 57.5 | 60.2 | 63.0 | 71.4 | 84.7 | 50.9 | 52.5 | 28.6 | 57.5 | 42.1 | 30.4 | 46.1 | 40.6 | 63.3 | | |
| CCNet [95] | IMP-ResNet-50 | 58.3 | 61.4 | 65.7 | 68.9 | 82.9 | 57.1 | 56.8 | 34.0 | 57.6 | 38.3 | 31.6 | 36.5 | 57.2 | 75.0 | | |
| EncNet [96] | IMP-ResNet-50 | 58.9 | 59.7 | 64.9 | 70.0 | 84.2 | 55.2 | 46.3 | 36.8 | 57.2 | 38.7 | 34.8 | 42.4 | 59.8 | 69.8 | | |
| HRNet [97] | IMP-HRNetW-18 | 61.5 | 65.9 | 68.9 | 74.0 | 86.9 | 59.4 | 61.5 | 33.8 | 62.1 | 46.9 | 14.9 | 44.2 | 52.9 | 75.6 | | |
| RANet [98] | IMP-ResNet-50 | 62.1 | 67.1 | 61.3 | 72.5 | 85.1 | 53.2 | 47.1 | 45.3* | 60.1 | 49.3 | 38.1 | 41.8 | 70.5 | 58.8 | | |
| AlignSeg [99] | IMP-ResNet-50 | 62.1 | 67.4 | 68.9 | 76.2 | 86.2 | 62.1 | 52.0 | 28.7 | 60.7 | 50.3 | 31.2 | 45.7 | 56.2 | 71.2 | | |
| OCR [100] | IMP-HRNetW-48 | 62.6 | 67.8 | 70.7 | 73.8 | 87.9 | 63.4 | 47.7 | 33.1 | 61.4 | 49.6 | 30.4 | 48.4 | 59.5 | 72.8 | | |
| HMANet [101] | IMP-ResNet-50 | 62.6 | 65.4 | 70.9 | 74.7 | 88.7 | 60.5 | 54.6 | 29.0 | 59.7 | 50.3 | 32.6 | 51.4 | 62.9 | 70.2 | | |
| FarSeg [102] | IMP-ResNet-50 | 63.7 | 65.4 | 61.8 | 77.7 | 86.4 | 62.1 | 56.7 | 36.7 | 60.6 | 46.3 | 35.8 | 51.2 | 71.4* | 72.5 | | |
| FactSeg [103] | IMP-ResNet-50 | 64.8 | 68.3 | 56.8 | 78.4* | 88.9* | 64.9* | 54.6 | 36.3 | 62.7 | 49.5 | 42.7 | 51.5* | 69.4 | 73.6 | | |
| UperNet | IMP-ResNet-50 | 61.9 | 65.9 | 73.9 | 68.1 | 70.7 | 57.3 | 52.5 | 39.2 | 61.2 | 48.8 | 34.3 | 44.5 | 62.1 | 76.8 | 83.8 | |
| UperNet | SeCo-ResNet-50 | 57.2 | 63.9 | 71.7 | 66.9 | 69.9 | 54.5 | 45.9 | 38.9 | 58.2 | 44.8 | 33.2 | 9.3 | 52.3 | 71.6 | 83.3 | |
| UperNet | RSP-ResNet-50 | 61.6 | 64.2 | 75.9 | 68.9 | 58.5 | 54.4 | 40.2 | 59.6 | 47.5 | 32.1 | 43.8 | 65.4 | 76.5 | 82.8 | 51.5 | |
| UperNet | IMP-Swin-T | 64.6 | 69.2 | 76.5 | 74.1 | 69.9 | 56.3 | 60.1 | 41.9 | 62.3 | 51.6 | 44.7* | 45.8 | 64.5 | 75.9 | 85.7 | 56.7 |
| UperNet | RSP-Swin-T | 64.1 | 67.0 | 74.6 | 73.7 | 70.7 | 59.0 | 60.1 | 44.3 | 62.0 | 50.6 | 37.6 | 46.8 | 64.9 | 76.2 | 85.2 | 53.8 |
| UperNet | IMP-ViTAEv2-S | 65.3* | 71.4* | 77.5* | 68.2 | 71.0 | 60.8 | 61.9 | 43.0 | 63.8* | 53.6* | 43.4 | 44.8 | 65.1 | 77.9* | 86.4* | 57.7* |
| UperNet | RSP-ViTAEv2-S | 64.3 | 71.3 | 74.3 | 72.2 | 70.4 | 57.4 | 63.0* | 44.0 | 62.5 | 51.6 | 35.4 | 47.0 | 62.2 | 77.7 | 85.2 | 54.7 |

¹ ST: storage tank. BD: baseball diamond. TC: tennis court. BC: baseball court. GTF: ground track field. LV: large vehicle. SV: small vehicle. HC: helicopter. SP: swimming pool. RA: roundabout. SBF: soccer ball field.

be improved. On the other hand, the IMP-Swin-T performs to be competitive and the IMP-ViTAEv2-S achieves the best performance on the iSAID dataset, outperforming the SOTA methods such as the HRNet [97] and OCR [100] as well as a series of methods that specially designed for aerial semantic segmentation, e.g., the FarSeg [102] and FactSeg [103].

Table VII also shows the advantages of RSP models are lying in the “Bridge” category, which conforms to the finding in the previous scene recognition task. Nevertheless, we can also see from Table VI-VII that, on the segmentation task, the performance of RSP are not as good as the classical IMP. In our considerations, there may be two reasons. The first one is the difference between the pretraining dataset and the evaluation one. Besides the dataset volume (note that the training sample and category numbers of MillionAID are smaller than ImageNet-1k), the spectral disparities also has a side impact on the performance, especially on the Potsdam dataset,

which adopts the IR-R-G channels instead of the ordinary RGB image (See Figure 5). The another reason we attribute to the difference between tasks. The representation used for scene recognition need to have the global understanding of the whole scene as Figure 4 shows, while the segmentation task requires the features to be more detailed while possessing high-level semantic information simultaneously, since they separately conduct the scene level or pixel level classification. To prove this conjecture, we then evaluate these networks on the aerial object detection task in next section. The granularity of the representation needed for detection probably lies between those for the segmentation and recognition tasks, since one of the aims in the detection task is the object-level classification.

Qualitative Results and Analyses: We present some visual segmentation results of the UperNet with different backbones on the Potsdam dataset in Figure 6. As can be seen, only the ViTAEv2-S successfully connects the long strip low veg-

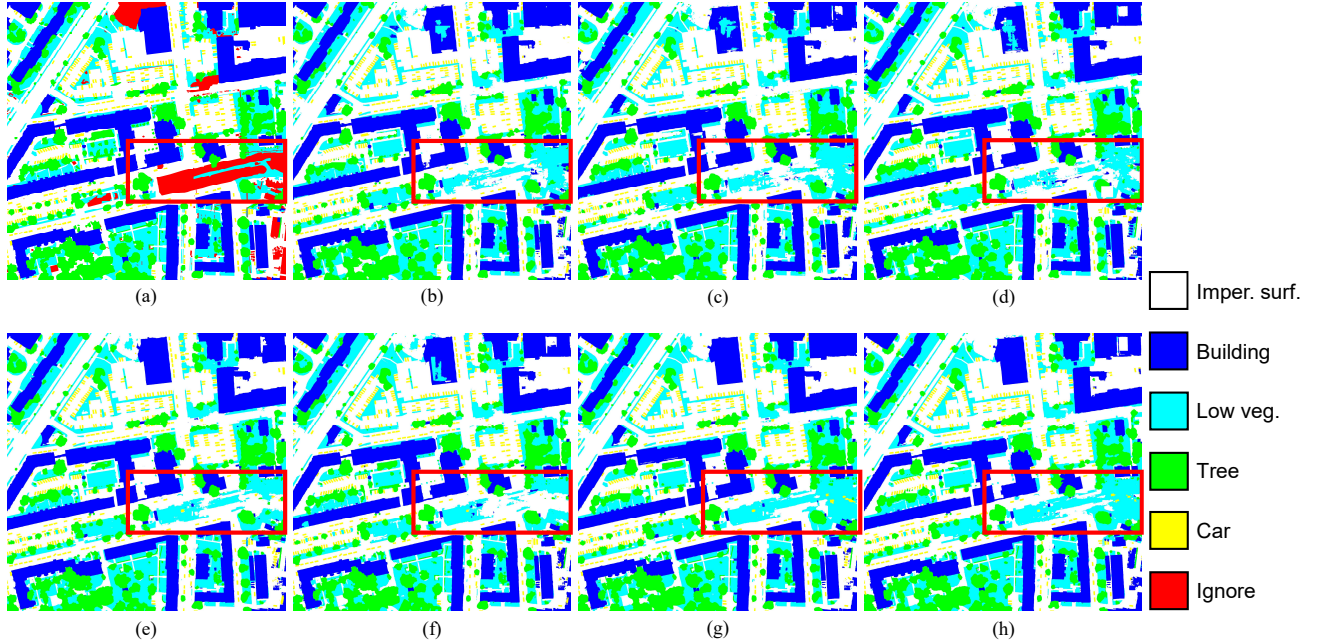


Fig. 6. Segmentation maps of the UperNet with different backbones on the Potsdam dataset. (a) Ground Truth. (b) IMP-ResNet-50. (c) SeCo-ResNet-50. (d) RSP-ResNet-50. (e) IMP-Swin-T. (f) RSP-Swin-T. (g) IMP-ViTAEv2-S. (h) RSP-ViTAEv2-S.

etations (see the red boxes), while IMP-ViTAEv2-S performs slightly better than RSP-ViTAEv2-S, which is consistent with the quantitative results in Table VI.

C. Aerial Object Detection

Since the aerial images are top down photoed in the sky, the objects can be presented as any directions in the birdview. Thus, the aerial object detection is the oriented bounding box (OBB) detection, which is distinguished to the usual horizontal bounding box (HBB) task on natural images [104]–[106]. In this paper, similar to segmentation, we also use different detection datasets in the experiments. Concretely, we evaluated on the multi-category remote sensing objects detection and the single-category ship detection subtasks, respectively.

1) Dataset: Two datasets including the large-scale DOTA [107] scenes and the commonly used HRSC2016 [108] dataset are separately utilized for the above objectives.

- **DOTA:** This is the most famous large-scale dataset for OBB detection. It totally contains 2,806 images whose size ranges from 800×800 to $4,000 \times 4,000$, where 188,282 instances belonging to 15 categories are included. The training, validation and testing set separately have 1,411/458/937 tiles. It should be noticed that the categories are completely same with the iSAID dataset, since the two datasets share the same set of scenes. The difference lies in the annotations for different tasks.
- **HRSC2016:** This is a specialized ship detection dataset, where the bounding boxes are annotated in arbitrary orientations. 1,061 images with the size ranging from 300×300 to $1,500 \times 900$ are included. In the official division, 436/181/444 images are used for training, validation and testing, respectively. The dataset only has one category, since there is no need to recognize the type of ships.

2) Implementation Detail and Experimental Setting: Similar to segmentation, the ResNet models are trained using the SGDM algorithm with the learning rate of 0.005, momentum of 0.9 and weight decay of 0.0001, while the vision transformers are trained with the AdamW optimizer, where the learning rate and weight decay are separately set to 0.0001 and 0.05. These models are trained for 12 and 36 epochs with a batchsize of 2 on DOTA and HRSC2016 scenes, respectively. The learning rate is adjusted by a multi-step scheduler. On DOTA dataset, the learning rate will be separately reduced by $10\times$ after the 8th epoch and the 11th epoch, while on HRSC2016 scene, the corresponded settings are epoch 24 and epoch 33. We use one of the SOTA OBB detection frameworks — ORCN [109] to evaluate the performance of different pretrained backbones. We adopt the default hyper-parameters of ORCN, which is implemented in OBBDetection². Following [109], the DOTA dataset is sampled and cropped to $1,024 \times 1,024$ patches with a stride of 824, while the HRSC2016 images are scaled keeping the aspect ratio with the shorter side equals to 800, and the length of the longer side is less than or equal to 1333. Data augmentations during training include random horizontal and vertical flipping. For convenience, the original training and validation sets are merged together for training, while the original testing sets of DOTA and HRSC2016 are separately used for evaluation. We report the mean average precision (mAP) of all categories and the average precision (AP) of each class on the corresponding testing set. All models are trained on a single V100 GPU.

3) Experimental Results: Quantitative Results and Analyses: Table VIII-IX show the results of OBB detection experiments. On the challenging DOTA dataset, it can be seen that using the advanced ORCN framework, the models

²<https://github.com/jbwang1997/OBBDetection>

TABLE VIII

RESULTS OF THE ORCN DETECTION MODEL WITH DIFFERENT BACKBONES AND SOTA METHODS ON THE TESTING SET OF DOTA DATASET. †: THE RESULT IS FROM AERIALDETECTON [110]. ‡: THE RESULT IS FROM THE ORIGINAL ORCN PAPER.

| Method | Backbone | mAP | AP per category ¹ | | | | | | | | | | | | | | |
|---|--------------------|-------|------------------------------|--------|--------|--------|-------|--------|--------|-------|-------|--------|--------|--------|--------|--------|--------|
| | | | Ship | ST | BD | TC | BC | GTF | Bridge | LV | SV | HC | SP | RA | SBF | Plane | Harbor |
| One-stage | | | | | | | | | | | | | | | | | |
| RetinaNet [105] † | IMP-ResNet-50-FPN | 68.43 | 79.11 | 74.32 | 77.62 | 90.29 | 82.18 | 58.17 | 41.81 | 71.64 | 74.58 | 60.64 | 69.67 | 60.60 | 54.75 | 88.67 | 62.57 |
| DAL [111] | IMP-ResNet-50-FPN | 71.44 | 79.74 | 78.45 | 76.55 | 90.84 | 79.54 | 66.80 | 45.08 | 76.76 | 67.00 | 60.11 | 73.14 | 62.27 | 57.71 | 88.68 | 69.05 |
| RSDet [112] | IMP-ResNet-101-FPN | 72.20 | 70.20 | 83.40 | 82.90 | 90.50 | 85.60 | 65.20 | 48.60 | 70.10 | 69.50 | 68.00* | 67.20 | 63.90 | 62.50 | 89.80 | 65.60 |
| R3Det [113] | IMP-ResNet-101-FPN | 71.69 | 77.54 | 83.54 | 81.99 | 90.80 | 81.39 | 62.52 | 48.46 | 74.29 | 70.48 | 60.05 | 67.46 | 59.82 | 61.97 | 89.54 | 65.44 |
| R3Det [113] | IMP-ResNet-152-FPN | 73.74 | 78.21 | 84.23 | 81.17 | 90.81 | 85.26 | 66.10 | 50.53 | 78.66 | 70.92 | 67.17 | 69.83 | 63.77 | 61.81 | 89.49 | 68.16 |
| S ² ANet [114] | IMP-ResNet-50-FPN | 74.12 | 87.25 | 85.64 | 82.84 | 90.83 | 84.90 | 71.11 | 48.37 | 78.39 | 78.11 | 57.94 | 69.13 | 62.60 | 60.36 | 89.11 | 65.26 |
| S ² ANet [114] | IMP-ResNet-101-FPN | 76.11 | 88.04 | 86.22 | 81.41 | 90.69 | 84.75 | 69.75 | 54.28 | 80.54 | 78.04 | 58.86 | 73.37* | 65.81 | 65.03 | 88.70 | 76.16 |
| Two-stage | | | | | | | | | | | | | | | | | |
| ICN [115] | IMP-ResNet-101-FPN | 68.16 | 69.98 | 78.20 | 74.30 | 90.76 | 79.06 | 70.32 | 47.70 | 67.82 | 64.89 | 50.23 | 64.17 | 62.90 | 53.64 | 81.36 | 67.02 |
| Faster R-CNN [104] † | IMP-ResNet-50-FPN | 69.05 | 77.11 | 83.90 | 73.06 | 90.84 | 78.94 | 59.09 | 44.86 | 71.49 | 73.25 | 56.18 | 64.91 | 62.95 | 48.59 | 88.44 | 62.18 |
| CAD-Net [116] | IMP-ResNet-101-FPN | 69.90 | 76.60 | 73.30 | 82.40 | 90.90* | 79.20 | 73.50 | 49.40 | 63.50 | 71.10 | 62.20 | 60.90 | 48.40 | 87.80 | 62.00 | |
| ROI Transformer [117] | IMP-ResNet-101-FPN | 69.56 | 83.59 | 81.46 | 78.52 | 90.74 | 77.27 | 75.92 | 43.44 | 73.68 | 68.81 | 47.67 | 58.93 | 53.54 | 58.39 | 88.64 | 62.83 |
| SCRDet [118] | IMP-ResNet-101-FPN | 72.61 | 72.41 | 86.86* | 80.65 | 90.85 | 87.94 | 68.36 | 52.09 | 60.32 | 68.36 | 65.21 | 68.24 | 66.68 | 65.02 | 89.98 | 66.25 |
| ROI Transformer † [117] | IMP-ResNet-50-FPN | 74.61 | 86.87 | 82.51 | 82.60 | 90.71 | 83.83 | 70.87 | 52.53 | 76.67 | 77.93 | 61.03 | 68.75 | 67.61 | 53.95 | 88.65 | 74.67 |
| Gliding Vertex [119] | IMP-ResNet-101-FPN | 75.02 | 86.82 | 86.81 | 85.00 | 90.74 | 79.02 | 77.34* | 52.26 | 73.14 | 73.01 | 57.32 | 70.86 | 70.91* | 59.55 | 89.64 | 72.94 |
| FAOD [120] | IMP-ResNet-101-FPN | 73.28 | 79.56 | 84.68 | 79.58 | 90.83 | 83.40 | 76.41 | 45.49 | 68.27 | 73.18 | 64.86 | 69.69 | 65.42 | 53.40 | 90.21* | 74.17 |
| CenterMap-Net [121] | IMP-ResNet-50-FPN | 71.74 | 78.10 | 83.61 | 81.24 | 88.83 | 77.80 | 60.65 | 53.15 | 66.55 | 78.62 | 58.70 | 72.36 | 66.19 | 49.36 | 88.88 | 72.10 |
| FR-Est [122] | IMP-ResNet-101-FPN | 74.20 | 86.44 | 83.56 | 81.17 | 90.82 | 84.13 | 70.19 | 50.44 | 77.98 | 73.52 | 60.55 | 66.72 | 66.59 | 60.64 | 89.63 | 70.59 |
| Mask OBB [123] | IMP-ResNet-50-FPN | 74.86 | 85.57 | 85.05 | 85.09* | 90.37 | 82.08 | 72.90 | 51.85 | 73.23 | 75.28 | 66.33 | 69.87 | 68.39 | 55.73 | 89.61 | 71.61 |
| ORCN ‡ [109] | IMP-ResNet-50-FPN | 75.87 | 88.20* | 84.68 | 82.12 | 90.90* | 87.50 | 70.86 | 54.78 | 83.00 | 78.93 | 52.28 | 68.84 | 67.69 | 63.97 | 89.46 | 74.94 |
| ORCN ‡ [109] | IMP-ResNet-101-FPN | 76.28 | 87.52 | 85.33 | 83.48 | 90.90* | 85.56 | 76.92 | 55.27 | 82.10 | 74.27 | 57.28 | 70.15 | 66.82 | 65.51* | 88.86 | 74.36 |
| 1 ST: storage tank. BD: baseball diamond. TC: tennis court. BC: baseball court. GTF: ground track field. LV: large vehicle. SV: small vehicle. HC: helicopter. SP: swimming pool. RA: roundabout. SBF: soccer ball field. | | | | | | | | | | | | | | | | | |

TABLE IX

RESULTS OF THE ORCN DETECTION MODEL WITH DIFFERENT BACKBONES AND SOTA METHODS ON THE TESTING SET OF HRSC2016 DATASET. †: THE RESULT IS FROM THE ORIGINAL ORCN PAPER.

| Method | Backbone | mAP |
|---------------------------|--------------------|-------|
| R2PN [124] | IMP-VGG-16 | 79.6 |
| RRD [125] | IMP-VGG-16 | 84.3 |
| FoRDet [126] | IMP-VGG-16 | 89.9 |
| R2CNN [127] | IMP-ResNet-101 | 73.1 |
| Rotated RPN [128] | IMP-ResNet-101 | 79.1 |
| ROI Transformer [117] | IMP-ResNet-101-FPN | 86.2 |
| Gliding Vertex [119] | IMP-ResNet-101-FPN | 88.2 |
| GRS-Det [129] | IMP-ResNet-50-FPN | 88.9 |
| GRS-Det [129] | IMP-ResNet-101-FPN | 89.6 |
| R3Det [113] | IMP-ResNet-101-FPN | 89.3 |
| DAL [111] | IMP-ResNet-101-FPN | 89.8 |
| AProNet [114] | IMP-ResNet-101-FPN | 90.0 |
| S ² ANet [114] | IMP-ResNet-101-FPN | 90.2 |
| ORCN † [109] | IMP-ResNet-50-FPN | 90.4* |
| ORCN | IMP-ResNet-50-FPN | 90.4* |
| ORCN | SeCo-ResNet-50-FPN | 88.9 |
| ORCN | RSP-ResNet-50-FPN | 90.3 |
| ORCN | IMP-Swin-T-FPN | 89.7 |
| ORCN | RSP-Swin-T-FPN | 90.0 |
| ORCN | IMP-ViTAEv2-S-FPN | 90.4* |
| ORCN | RSP-ViTAEv2-S-FPN | 90.4* |

whose backbone is either ResNet-50 or Swin-T performs well, although the mAPs of Swin-T models are slightly lower than the ResNet models. The ViTAEv2-S, which is a kind of vision transformer network that is introduced the inductive biases including the locality and scale-invariance characteristics of CNN, obtains amazing performance that improve the ORCN baseline by nearly 2% mAP. Another point needed to be noticed is the performance of RSP weights on these three backbones all outperforms their ImageNet pretrained counterparts. These results support our previous claims that the granularity of the representation required for the detection task is more closer to that for the scene recognition task compared with the segmentation task. Thus, the performance difference between RSP and IMP in the detection experiments aligns with the

results in the scene recognition experiments.

In addition, we observe that compared with IMP-ViTAEv2-S, the APs of most categories obtained by RSP-ViTAEv2-S are smaller, implying the universality of IMP. Nevertheless, the mAP of RSP-ViTAEv2-S is higher than IMP-ViTAEv2-S, since RSP has significant advantages on the categories of “Bridge” and aerial vehicles including “Helicopter” or “Plane”, echoing the previous finding in the segmentation experiments. While on the other categories, the gaps between these two models are not very large. Combining the above two points, RSP-ViTAEv2-S delivers better overall performance than IMP-ViTAEv2-S. On HRSC2016 dataset, the results of RSP and IMP are roughly the same, where there are win or lose on both sides. Compared with CNN, the vision transformer models have not demonstrated the advantages. We think that on this relatively easy subtask, where only one category needed to be detected and the ship sizes in HRSC2016 are relatively larger than DOTA, the performance is probably saturated.

Qualitative Results and Analyses: We visualize some detection results of the ORCN model with the ViTAEv2-S backbones on the DOTA testing set in Figure 7. The red boxes show that, when objects are densely distributed, the RSP-ViTAEv2-S can still predict correct object categories, while the IMP-ViTAEv2-S is confused by the dense context and makes wrong predictions. For the “Bridge” category, the IMP-ViTAEv2-S produces missing detections (see yellow boxes), while the RSP-ViTAEv2-S model successfully detect the long bridge with a high confidence score.

D. Aerial Change Detection

We then apply the above models on a typical application in the remote sensing field, i.e., change detection, which aims to find the changes between two aerial images of a same region

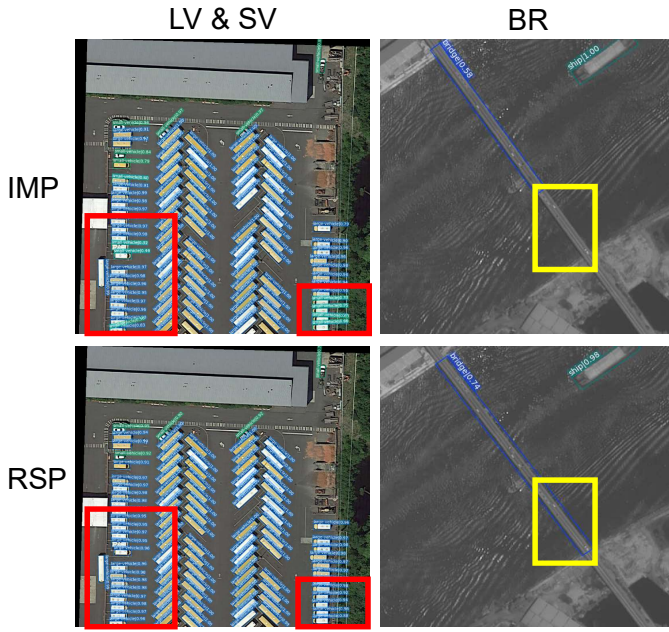


Fig. 7. Visual detection results of the ORCN model with the ViTAEv2-S backbones on the DOTA testing set. LV: large vehicle. SV: small vehicle. BR: Bridge. IMP: IMP-ViTAEv2-S. RSP: RSP-ViTAEv2-S.

captured at different time. It is formulated as a pixel-level binary classification task, where “1” indicates change.

1) *Dataset*: We adopt the commonly used CDD [130] and LEVIR [131] datasets to comprehensively evaluate the above models on this task, since they separately involve the natural and artificial changes.

- CDD: The original dataset contains 11 pairs of multi-source real season-varying remote sensing images collecting from GE, where 7 pairs of images are at the size of $4,725 \times 2,200$ and 4 image pairs are at the size of $1,900 \times 1,000$ pixels. The resolutions are ranging from 0.03m to 1m. Then, [132] clipped the images to a series of 256×256 patches and generated a dataset, where the sizes of the training, validation and testing set are 10,000/3,000/3,000, respectively.
- LEVIR: This dataset is collected using the GE API on 20 different regions in Texas, USA from 2002 to 2018. It contains 637 image pairs at the size of $1,024 \times 1,024$ and with a high resolution of 0.5m, where most changes are from man-made structures, including 31,333 independent building change entities. The training, validation and testing set contain 445/64/128 image pairs, respectively.

2) *Implementation Detail and Experimental Setting*: In this section, we adopt a SOTA framework — BIT [133], which uses the transformer to capture the contextual information between different temporal images for change detection. If BIT is equipped with the ResNet backbone, it is optimized by the SGDM optimizer, where the learning rate, momentum and weight decay are 0.001, 0.99 and 0.0005. While the Swin or ViTAE based BIT models are trained with the AdamW optimizer with the learning rate of 6e-5 and weight decay of 0.01. These models are trained for 200 epochs with a batchsize of 8, while the learning rate is linearly decayed

TABLE X

RESULTS OF THE BIT CHANGE DETECTION MODEL WITH DIFFERENT BACKBONES AND SOTA METHODS ON THE TESTING SET OF CDD AND LEVIR DATASETS. †: THE RESULT IS FROM THE ORIGINAL BIT PAPER.

| Method | Backbone | F1 score | |
|--------------------|-----------------------|---------------|---------------|
| | | CDD | LEVIR |
| FC-EF [134] | — | 77.11 | 62.32 |
| FC-Siam-conc [134] | — | 82.50 | 68.21 |
| FC-Siam-diff [134] | — | 83.73 | 63.09 |
| CLNet [135] | — | 92.10 | 90.00 |
| SNUNet-c48 [136] | — | 96.20 | — |
| IFN [137] | IMP-VGG-16 | 90.30 | 83.57 |
| DASNet [138] | IMP-VGG-16 | 91.93 | 82.83 |
| SRCDNet [139] | IMP-ResNet-18 | 90.02 | — |
| STANet [131] | IMP-ResNet-18 | 90.75 | 87.34 |
| BSFNet [140] | IMP-ResNet-18 | 91.90 | 88.00 |
| DSAMNet [141] | IMP-ResNet-18 | 93.69 | — |
| HRTNet [142] | IMP-HRNet-W18 | 93.71 | 88.48 |
| CDNet+IAug [143] | IMP-ResNet-18 | — | 89.00 |
| BIT† [133] | IMP-ResNet-18 | — | 89.31 |
| ChangeFormer [144] | IMP-MiT-B2 [39] | — | 90.40 |
| CS-HSNet [145] | IMP-ResNet-50 | 94.95 | 90.79 |
| LSS-Net [146] | IMP-SE-ResNet-50 | 96.30 | — |
| ChangeStar [147] | IMP-ResNext-101-32×4d | — | 91.25 |
| BIT | IMP-ResNet-50 | 95.09 | 89.19 |
| BIT | SeCo-ResNet-50 | 95.95 | 90.14 |
| BIT | RSP-ResNet-50 | 96.00 | 90.10 |
| BIT | IMP-Swin-T | 94.77 | 90.25 |
| BIT | RSP-Swin-T | 95.21 | 90.10 |
| BIT | IMP-ViTAEv2-S | 97.02* | 91.26* |
| BIT | RSP-ViTAEv2-S | 96.81 | 90.93 |

until the end of training. Following [133], the LEVIR dataset is clipped to the patches at the size of 256×256 with no overlaps. Thus, the sizes of training, validation and testing set are 7,120/1,024/2,048. The final performance of different models is evaluated on the testing set, while the results on the validation set are only used to select the best model during training. We use the F1 score as the evaluation metric and the experiments are conducted on a single V100 GPU.

3) *Experimental Results: Quantitative Results and Analyses*: The quantitative results are summarized in Table X. Without surprise, the self-supervised SeCo pretrained weights perform well on this task, e.g., the SeCo-ResNet-50 based BIT performs better than the IMP counterpart. Although the SeCo weights are trained to achieve seasonal-invariance, the change features can be encoded via the multi-head sub-space embedding [50]. Nevertheless, ViTAEv2-S pretrained either by IMP or RSP performs better than SeCo-ResNet-50, showing the benefit of using the advanced backbone.

Compared with other methods, it is no doubt that the ViTAEv2-S achieve the best performance, showing the potentiality of applying advanced vision transformer on remote sensing field. As before, we analyse the performance difference between the RSP with the IMP through the perspective of task characteristics. Given the analyses in previous sections, we can infer that the granularity of the required representation for the change detection lies in between those of the segmentation and detection, since it is also a segmentation task, although there only are two categories and there is no need to recognize specific object category.

Qualitative Results and Analyses: We present some visual change detection results in Figure 8. As can be seen, ResNet-50 and Swin-T by IMP can not well detect the changes of roads inside the fields in the natural scene. This issue could be partly alleviated by adopting RSP. It is consistent with

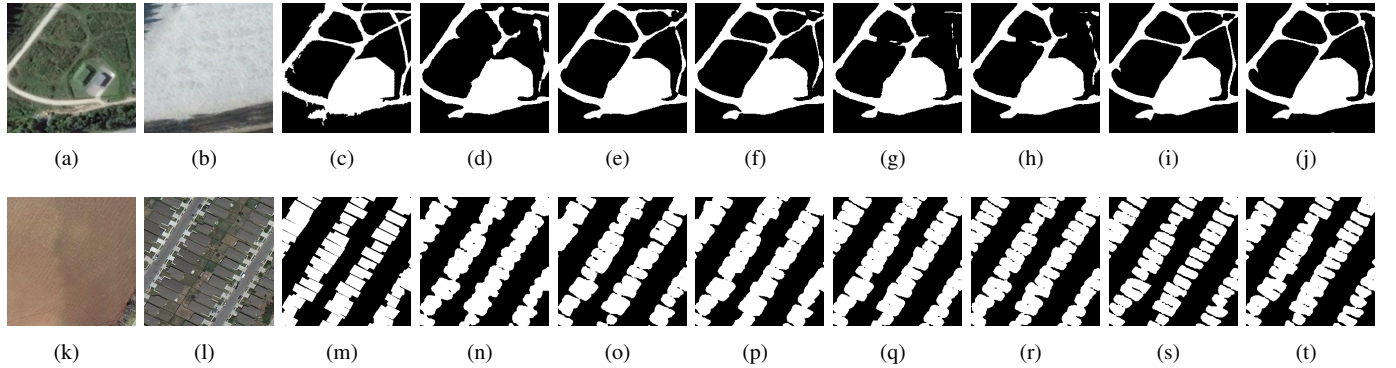


Fig. 8. Visual change detection results. The first and second row separately show the change detection results of a sample image from the CDD and LEVIR datasets. Here, (a) and (k), (b) and (l) are the first and second temporals of the same regions. (c) and (m) are ground truth change annotations. (d) and (n) are the results of the IMP-ResNet-50 based BIT, while (e) and (o), (f) and (p), (g) and (q), (h) and (r), (i) and (s), (g) and (t) are the results from the SeCo-ResNet-50, RSP-ResNet-50, IMP-Swin-T, RSP-Swin-T, IMP-ViTAEv2-S, and RSP-ViTAEv2-S backbones, respectively.

TABLE XI

OVERALL COMPARISONS OF DIFFERENT BACKBONES TRAINED WITH DIFFERENT EPOCHS ON ALL DOWNSTREAM TASKS.

| Backbone | Scene Recognition | Semantic Segmentation | Object Detection | Change Detection |
|--------------------|-------------------|-----------------------|------------------|------------------|
| RSP-ResNet-50-E120 | 96.53 | 75.70 | 82.51 | 92.82 |
| RSP-ResNet-50-E300 | 96.63 | 75.68 | 83.39 | 93.05 |
| RSP-Swin-T-E120 | 96.06 | 76.17 | 83.08 | 92.28 |
| RSP-Swin-T-E300 | 96.44 | 77.07 | 82.80 | 92.66 |
| RSP-ViTAEv2-S-E40 | 96.76 | 76.95 | 83.65 | 93.08 |
| RSP-ViTAEv2-S-E100 | 97.01 | 77.45 | 83.98 | 93.87 |

the results in Table X that SeCo-ResNet-50 further improves the detection in the road areas. Compared with the above models, the ViTAEv2-S model effectively captures the road details. In the artificial changed scene, the ViTAEv2-S model greatly overcomes the problem of object adhesion in the results of all other models, demonstrating that the ViTAEv2-S features are more discriminative for distinguishing objects from background.

E. Overall Comparison of Different Backbones on All Tasks

In this part, we comprehensively compare the performance of different backbones by RSP on all tasks. Specifically, the scores in Table XI are calculated by averaging the scores across all datasets for each task. For example, we calculate the average score of the mean values on five settings in the scene recognition task, so the overall accuracy of RSP-ResNet-50-E120 is $(99.52+96.60+97.78+93.76+94.97)/5 \approx 96.53$, while the overall score of RSP-Swin-T-E300 on the segmentation task is obtained by averaging the mF1 on Potsdam dataset and the mIOU on iSAID dataset: $(90.03+64.10)/2 \approx 77.07$. From Table XI, we can find that, the backbones pretraining with more epochs generally perform better on downstream tasks, since they obtain stronger representations, although there is an exception, i.e., the Swin-T on the object detection task, implying the task discrepancy also matters. In general, ViTAEv2-S that takes advantages of CNN and transformers delivers better performance when training with more epochs, and outperforms ResNet-50 and Swin-T on all the tasks.

V. CONCLUSION

In this study, we investigate the remote sensing pretraining problem based on both CNN and vision transformers on the largest remote sensing dataset MillionAID, and comprehensively evaluate their performance on four related tasks, including scene recognition, semantic segmentation, object detection, and change detection, as well as compare them with the ImageNet pretraining and other SOTA methods. By synthetically analysing the experiment results, we draw the following conclusions:

- Compared with the traditional CNN model, the vision transformers perform competitively on a series of remote sensing tasks, and they can obtain better performance on some more challenging datasets, such as the iSAID and DOTA. Particularly, the ViTAEv2-S, an advanced model introducing the inductive biases of CNN into the vision transformers, achieves the best performance on almost all settings of these tasks.
- Benefiting from the large capacity of ImageNet-1K dataset, the classical IMP enables deep models to learn more universal representations that generalize well to almost all categories in the downstream tasks. Thus, the IMP can produce competitive baseline results despite on aerial scenes. RSP is comparable with IMP and performs extremely well on some specific categories, such as the “Bridge” and “Airplane”, owing to mitigating the data-level discrepancy between the upstream pretraining task and downstream task.
- The task-level discrepancy also has a side impact on the performance of RSP. If the granularity of the representation required for a specific downstream task is closer to that of the upstream pretraining task, i.e., scene recognition, RSP usually leads to a better performance.

We hope this study can provide useful insights to the community about using advanced vision transformers and remote sensing pretraining. In future work, we will investigate the RSP on large-scale datasets for downstream tasks as well as the unsupervised pretraining considering the abundant unlabelled data in this area.

REFERENCES

- [1] X. Zhang, Y. Sun, K. Shang, L. Zhang, and S. Wang, "Crop classification based on feature band set construction and object-oriented approach using hyperspectral images," *IEEE J. Sel. Topics Appl. Earth Observ. Remote Sens.*, vol. 9, no. 9, pp. 4117–4128, Sep. 2016.
- [2] J. Zhang and D. Tao, "Empowering things with intelligence: a survey of the progress, challenges, and opportunities in artificial intelligence of things," *IEEE Internet of Things Journal*, vol. 8, no. 10, pp. 7789–7817, 2020.
- [3] X. Yang and Y. Yu, "Estimating soil salinity under various moisture conditions: An experimental study," *IEEE Trans. Geosci. Remote Sens.*, vol. 55, no. 5, pp. 2525–2533, May 2017.
- [4] M. J. Swain and D. H. Ballard, "Color indexing," *Int. J. Comput. Vis.*, vol. 7, no. 1, pp. 11–32, 1991.
- [5] R. M. Haralick, K. Shanmugam, and I. Dinstein, "Textural features for image classification," *IEEE Trans. Syst. Man Cybern.*, vol. SMC-3, no. 6, pp. 610–621, 1973.
- [6] A. Oliva and A. Torralba, "Modeling the shape of the scene: A holistic representation of the spatial envelope," *Int. J. Comput. Vis.*, vol. 42, no. 3, pp. 145–175, 2001.
- [7] O. A. Penatti, K. Nogueira, and J. A. Dos Santos, "Do deep features generalize from everyday objects to remote sensing and aerial scenes domains?" in *CVPRW*, 2015, pp. 44–51.
- [8] Y. Bengio, A. Courville, and P. Vincent, "Representation learning: A review and new perspectives," *IEEE Trans. Pattern Anal. Mach. Intell.*, vol. 35, no. 8, pp. 1798–1828, Aug 2013.
- [9] T. Hofmann, "Unsupervised learning by probabilistic latent semantic analysis," *Mach. Learn.*, vol. 42, no. 1, pp. 177–196, 2001.
- [10] J. Philbin, O. Chum, M. Isard, J. Sivic, and A. Zisserman, "Object retrieval with large vocabularies and fast spatial matching," in *CVPR*. IEEE, 2007, pp. 1–8.
- [11] K. Simonyan and A. Zisserman, "Very deep convolutional networks for large-scale image recognition," in *ICLR*, May 2015.
- [12] K. He, X. Zhang, S. Ren, and J. Sun, "Deep residual learning for image recognition," in *CVPR*, 2016, pp. 770–778.
- [13] Z. Liu, Y. Lin, Y. Cao, H. Hu, Y. Wei, Z. Zhang, S. Lin, and B. Guo, "Swin transformer: Hierarchical vision transformer using shifted windows," in *ICCV*, 2021, pp. 10012–10022.
- [14] Y. Xu, Q. Zhang, J. Zhang, and D. Tao, "Vitae: Vision transformer advanced by exploring intrinsic inductive bias," *NeurIPS*, vol. 34, 2021.
- [15] T. Xiao, Y. Liu, B. Zhou, Y. Jiang, and J. Sun, "Unified perceptual parsing for scene understanding," in *ECCV*, 2018, pp. 418–434.
- [16] Q. Zhang, J. Zhang, W. Liu, and D. Tao, "Category anchor-guided unsupervised domain adaptation for semantic segmentation," in *NeurIPS*, vol. 32, 2019.
- [17] L. Gao, J. Zhang, L. Zhang, and D. Tao, "Dsp: Dual soft-paste for unsupervised domain adaptive semantic segmentation," in *ACM Multimedia*, 2021, pp. 2825–2833.
- [18] D. Wang, B. Du, L. Zhang, and Y. Xu, "Adaptive spectral-spatial multiscale contextual feature extraction for hyperspectral image classification," *IEEE Trans. Geosci. Remote Sens.*, vol. 59, no. 3, pp. 2461–2477, 2021.
- [19] L. Zhang, M. Lan, J. Zhang, and D. Tao, "Stagewise unsupervised domain adaptation with adversarial self-training for road segmentation of remote-sensing images," *IEEE Trans. Geosci. Remote Sens.*, vol. 60, pp. 1–13, 2022.
- [20] D. Wang, B. Du, and L. Zhang, "Fully contextual network for hyperspectral scene parsing," *IEEE Trans. Geosci. Remote Sens.*, vol. 60, pp. 1–16, 2022.
- [21] G. Cheng, J. Han, and X. Lu, "Remote sensing image scene classification: Benchmark and state of the art," *Proc. IEEE*, vol. 105, no. 10, pp. 1865–1883, 2017.
- [22] J. Deng, W. Dong, R. Socher, L.-J. Li, K. Li, and L. Fei-Fei, "Imagenet: A large-scale hierarchical image database," in *CVPR*, 2009, pp. 248–255.
- [23] K. Xu, H. Huang, P. Deng, and Y. Li, "Deep feature aggregation framework driven by graph convolutional network for scene classification in remote sensing," *IEEE Trans. Neural Netw. Learn. Syst.*, 2021.
- [24] H. Sun, S. Li, X. Zheng, and X. Lu, "Remote sensing scene classification by gated bidirectional network," *IEEE Trans. Geosci. Remote Sens.*, vol. 58, no. 1, pp. 82–96, 2019.
- [25] Q. Zhao, Y. Ma, S. Lyu, and L. Chen, "Embedded self-distillation in compact multibranch ensemble network for remote sensing scene classification," *IEEE Trans. Geosci. Remote Sens.*, vol. 60, pp. 1–15, 2022.
- [26] Q. Zhao, S. Lyu, Y. Li, Y. Ma, and L. Chen, "Mgml: Multigranularity multilevel feature ensemble network for remote sensing scene classification," *IEEE Trans. Neural Netw. Learn. Syst.*, 2021.
- [27] Y. Long, G.-S. Xia, S. Li, W. Yang, M. Y. Yang, X. X. Zhu, L. Zhang, and D. Li, "On creating benchmark dataset for aerial image interpretation: Reviews, guidances and million-aid," *IEEE J. Sel. Topics Appl. Earth Observ. Remote Sens.*, vol. 14, pp. 4205–4230, 2021.
- [28] Q. Zhang, Y. Xu, J. Zhang, and D. Tao, "VitaeV2: Vision transformer advanced by exploring inductive bias for image recognition and beyond," *arXiv preprint arXiv:2202.10108*, 2022.
- [29] X. Wang, S. Wang, C. Ning, and H. Zhou, "Enhanced feature pyramid network with deep semantic embedding for remote sensing scene classification," *IEEE Trans. Geosci. Remote Sens.*, vol. 59, no. 9, pp. 7918–7932, 2021.
- [30] G. Huang, Z. Liu, L. Van Der Maaten, and K. Q. Weinberger, "Densely connected convolutional networks," in *CVPR*, 2017, pp. 4700–4708.
- [31] Q. Bi, K. Qin, H. Zhang, and G.-S. Xia, "Local semantic enhanced convnet for aerial scene recognition," *IEEE Trans. Image Process.*, vol. 30, pp. 6498–6511, 2021.
- [32] B. Ma, J. Zhang, Y. Xia, and D. Tao, "Auto learning attention," in *NeurIPS*, vol. 33, 2020, pp. 1488–1500.
- [33] S.-B. Chen, Q.-S. Wei, W.-Z. Wang, J. Tang, B. Luo, and Z.-Y. Wang, "Remote sensing scene classification via multi-branch local attention network," *IEEE Trans. Image Process.*, vol. 31, pp. 99–109, 2021.
- [34] S. Woo, J. Park, J.-Y. Lee, and I. S. Kweon, "Cbam: Convolutional block attention module," in *ECCV*, 2018, pp. 3–19.
- [35] Q. Bi, K. Qin, Z. Li, H. Zhang, K. Xu, and G.-S. Xia, "A multiple-instance densely-connected convnet for aerial scene classification," *IEEE Trans. Image Process.*, vol. 29, pp. 4911–4926, 2020.
- [36] A. Dosovitskiy, L. Beyer, A. Kolesnikov, D. Weissenborn, X. Zhai, T. Unterthiner, M. Dehghani, M. Minderer, G. Heigold, S. Gelly, J. Uszkoreit, and N. Houlsby, "An image is worth 16x16 words: Transformers for image recognition at scale," *ICLR*, 2021.
- [37] H. Touvron, M. Cord, M. Douze, F. Massa, A. Sablayrolles, and H. Jégou, "Training data-efficient image transformers & distillation through attention," in *ICML*. PMLR, 2021, pp. 10347–10357.
- [38] W. Wang, E. Xie, X. Li, D.-P. Fan, K. Song, D. Liang, T. Lu, P. Luo, and L. Shao, "Pyramid vision transformer: A versatile backbone for dense prediction without convolutions," in *ICCV*, 2021, pp. 568–578.
- [39] E. Xie, W. Wang, Z. Yu, A. Anandkumar, J. M. Alvarez, and P. Luo, "Segformer: Simple and efficient design for semantic segmentation with transformers," *NeurIPS*, vol. 34, 2021.
- [40] W. Wang, Y. Cao, J. Zhang, F. He, Z.-J. Zha, Y. Wen, and D. Tao, "Exploring sequence feature alignment for domain adaptive detection transformers," in *ACM Multimedia*, 2021, pp. 1730–1738.
- [41] W. Wang, Y. Cao, J. Zhang, and D. Tao, "FP-DETR: Detection transformer advanced by fully pre-training," in *ICLR*, 2022.
- [42] W. Wang, J. Zhang, Y. Cao, Y. Shen, and D. Tao, "Towards data-efficient detection transformers," *arXiv preprint arXiv:2203.09507*, 2022.
- [43] Z. Chen, J. Zhang, and D. Tao, "Recurrent glimpse-based decoder for detection with transformer," *arXiv preprint arXiv:2112.04632*, 2021.
- [44] P. Deng, K. Xu, and H. Huang, "When cnns meet vision transformer: A joint framework for remote sensing scene classification," *IEEE Geosci. Remote Sens. Lett.*, vol. 19, pp. 1–5, 2022.
- [45] W. Li, K. Chen, H. Chen, and Z. Shi, "Geographical knowledge-driven representation learning for remote sensing images," *IEEE Trans. Geosci. Remote Sens.*, vol. 60, pp. 1–16, 2022.
- [46] T. Chen, S. Kornblith, M. Norouzi, and G. Hinton, "A simple framework for contrastive learning of visual representations," in *ICML*. PMLR, 2020, pp. 1597–1607.
- [47] X. Chen, H. Fan, R. Girshick, and K. He, "Improved baselines with momentum contrastive learning," *arXiv preprint arXiv:2003.04297*, 2020.
- [48] Y. Xu, Q. Zhang, J. Zhang, and D. Tao, "Regioncl: Can simple region swapping contribute to contrastive learning?" *arXiv preprint arXiv:2111.12309*, 2021.
- [49] K. He, X. Chen, S. Xie, Y. Li, P. Dollár, and R. Girshick, "Masked autoencoders are scalable vision learners," *arXiv:2111.06377*, 2021.
- [50] O. Mañas, A. Lacoste, X. Giro-i Nieto, D. Vazquez, and P. Rodriguez, "Seasonal contrast: Unsupervised pre-training from uncurated remote sensing data," in *ICCV*, 2021, pp. 9414–9423.
- [51] J. Kang, R. Fernandez-Beltran, P. Duan, S. Liu, and A. J. Plaza, "Deep Unsupervised Embedding for Remotely Sensed Images Based on Spatially Augmented Momentum Contrast," *IEEE Trans. Geosci. Remote Sens.*, vol. 59, no. 3, pp. 2598–2610, Mar. 2021.

- [52] K. Ayush, B. Uzkent, C. Meng, K. Tanmay, M. Burke, D. Lobell, and S. Ermon, “Geography-aware self-supervised learning,” in *ICCV*, 2021, pp. 10 181–10 190.
- [53] S. Vincenzi, A. Porrello, P. Buzzega, M. Cipriano, P. Fronte, R. Cuccu, C. Ippoliti, A. Conte, and S. Calderara, “The color out of space: learning self-supervised representations for earth observation imagery,” in *ICPR*. IEEE, 2021, pp. 3034–3041.
- [54] G. Christie, N. Fendley, J. Wilson, and R. Mukherjee, “Functional map of the world,” in *CVPR*, 2018, pp. 6172–6180.
- [55] G. Sumbul, M. Charfuelan, B. Demir, and V. Markl, “Bigearthnet: A large-scale benchmark archive for remote sensing image understanding,” in *IGARSS*. IEEE, 2019, pp. 5901–5904.
- [56] L. Yuan, Y. Chen, T. Wang, W. Yu, Y. Shi, Z.-H. Jiang, F. E. Tay, J. Feng, and S. Yan, “Tokens-to-token vit: Training vision transformers from scratch on imagenet,” in *ICCV*, 2021, pp. 558–567.
- [57] P. Ramachandran, B. Zoph, and Q. V. Le, “Searching for activation functions,” *arXiv preprint arXiv:1710.05941*, 2017.
- [58] S. Ioffe and C. Szegedy, “Batch normalization: accelerating deep network training by reducing internal covariate shift,” in *ICML*, 2015.
- [59] E. D. Cubuk, B. Zoph, D. Mane, V. Vasudevan, and Q. V. Le, “Autoaugment: Learning augmentation policies from data,” *arXiv preprint arXiv:1805.09501*, 2018.
- [60] Z. Zhong, L. Zheng, G. Kang, S. Li, and Y. Yang, “Random erasing data augmentation,” in *AAAI*, vol. 34, no. 07, 2020, pp. 13 001–13 008.
- [61] H. Zhang, M. Cisse, Y. N. Dauphin, and D. Lopez-Paz, “mixup: Beyond empirical risk minimization,” *ICLR*, 2018.
- [62] S. Yun, D. Han, S. J. Oh, S. Chun, J. Choe, and Y. Yoo, “Cutmix: Regularization strategy to train strong classifiers with localizable features,” in *ICCV*, 2019, pp. 6023–6032.
- [63] Y. Yang and S. Newsam, “Bag-of-visual-words and spatial extensions for land-use classification,” in *GEOProcessing*, 2010, p. 270–279.
- [64] G.-S. Xia, J. Hu, F. Hu, B. Shi, X. Bai, Y. Zhong, L. Zhang, and X. Lu, “Aid: A benchmark data set for performance evaluation of aerial scene classification,” *IEEE Trans. Geosci. Remote Sens.*, vol. 55, no. 7, pp. 3965–3981, 2017.
- [65] Z. Zhao, J. Li, Z. Luo, J. Li, and C. Chen, “Remote Sensing Image Scene Classification Based on an Enhanced Attention Module,” *IEEE Geosci. Remote Sens. Lett.*, vol. 18, no. 11, pp. 1926–1930, Nov. 2021.
- [66] X. Zhang, W. An, J. Sun, H. Wu, W. Zhang, and Y. Du, “Best Representation Branch Model for Remote Sensing Image Scene Classification,” *IEEE J. Sel. Topics Appl. Earth Observ. Remote Sens.*, vol. 14, pp. 9768–9780, Jan. 2021.
- [67] B. Li, Y. Guo, J. Yang, L. Wang, Y. Wang, and W. An, “Gated Recurrent Multiattention Network for VHR Remote Sensing Image Classification,” *IEEE Trans. Geosci. Remote Sens.*, vol. 60, p. 3093914, Jan. 2022.
- [68] S. Wang, Y. Ren, G. Parr, Y. Guan, and L. Shao, “Invariant Deep Compressible Covariance Pooling for Aerial Scene Categorization,” *IEEE Trans. Geosci. Remote Sens.*, vol. 59, no. 8, pp. 6549–6561, Aug. 2021.
- [69] Q. Wang, S. Liu, J. Chanussot, and X. Li, “Scene Classification With Recurrent Attention of VHR Remote Sensing Images,” *IEEE Trans. Geosci. Remote Sens.*, vol. 57, no. 2, pp. 1155–1167, Feb. 2019.
- [70] N. He, L. Fang, S. Li, J. Plaza, and A. Plaza, “Skip-connected covariance network for remote sensing scene classification,” *IEEE Trans. Neural Netw. Learn. Syst.*, vol. 31, no. 5, pp. 1461–1474, 2020.
- [71] F. Li, R. Feng, W. Han, and L. Wang, “High-Resolution Remote Sensing Image Scene Classification via Key Filter Bank Based on Convolutional Neural Network,” *IEEE Trans. Geosci. Remote Sens.*, vol. 58, no. 11, pp. 8077–8092, Nov. 2020.
- [72] S. Wang, Y. Guan, and L. Shao, “Multi-Granularity Canonical Appearance Pooling for Remote Sensing Scene Classification,” *IEEE Trans. Image Process.*, vol. 29, pp. 5396–5407, Jan. 2020.
- [73] G. Zhang, W. Xu, W. Zhao, C. Huang, E. N. Yk, Y. Chen, and J. Su, “A Multiscale Attention Network for Remote Sensing Scene Images Classification,” *IEEE J. Sel. Topics Appl. Earth Observ. Remote Sens.*, vol. 14, pp. 9530–9545, Jan. 2021.
- [74] A. Chattopadhyay, A. Sarkar, P. Howlader, and V. N. Balasubramanian, “Grad-cam++: Generalized gradient-based visual explanations for deep convolutional networks,” in *WACV*. IEEE, 2018, pp. 839–847.
- [75] S. Waqas Zamir, A. Arora, A. Gupta, S. Khan, G. Sun, F. Shahbaz Khan, F. Zhu, L. Shao, G.-S. Xia, and X. Bai, “isaид: A large-scale dataset for instance segmentation in aerial images,” in *CVPRW*, 2019, pp. 28–37.
- [76] M. Contributors, “MMSegmentation: Openmmlab semantic segmentation toolbox and benchmark,” <https://github.com/open-mmlab/mms Segmentation>, 2020.
- [77] E. Shelhamer, J. Long, and T. Darrell, “Fully convolutional networks for semantic segmentation,” *IEEE Trans. Pattern Anal. Mach. Intell.*, vol. 39, no. 4, pp. 640–651, 2017.
- [78] L. Mou, Y. Hua, and X. X. Zhu, “Relation matters: Relational context-aware fully convolutional network for semantic segmentation of high-resolution aerial images,” *IEEE Trans. Geosci. Remote Sens.*, vol. 58, no. 11, pp. 7557–7569, 2020.
- [79] Y. Sun, X. Zhang, Q. Xin, and J. Huang, “Developing a multi-filter convolutional neural network for semantic segmentation using high-resolution aerial imagery and LiDAR data,” *ISPRS J. Photogramm. Remote Sens.*, vol. 143, pp. 3–14, Sep. 2018.
- [80] J. Fu, J. Liu, H. Tian, Y. Li, Y. Bao, Z. Fang, and H. Lu, “Dual attention network for scene segmentation,” in *CVPR*, 2019, pp. 3141–3149.
- [81] H. Zhao, J. Shi, X. Qi, X. Wang, and J. Jia, “Pyramid scene parsing network,” in *CVPR*, 2017, pp. 6230–6239.
- [82] L.-C. Chen, Y. Zhu, G. Papandreou, F. Schroff, and H. Adam, “Encoder-decoder with atrous separable convolution for semantic image segmentation,” in *ECCV*, 2018, pp. 801–818.
- [83] Q. Zhang and Y.-B. Yang, “Rest: An efficient transformer for visual recognition,” *NeurIPS*, vol. 34, 2021.
- [84] X. Zheng, L. Huan, G.-S. Xia, and J. Gong, “Parsing very high resolution urban scene images by learning deep ConvNets with edge-aware loss,” *ISPRS J. Photogramm. Remote Sens.*, vol. 170, pp. 15–28, Dec. 2020.
- [85] A. Srinivas, T.-Y. Lin, N. Parmar, J. Shlens, P. Abbeel, and A. Vaswani, “Bottleneck transformers for visual recognition,” in *CVPR*, 2021, pp. 16 519–16 529.
- [86] L. Ding, H. Tang, and L. Bruzzone, “LANet: Local Attention Embedding to Improve the Semantic Segmentation of Remote Sensing Images,” *IEEE Trans. Geosci. Remote Sens.*, vol. 59, no. 1, pp. 426–435, Jan. 2021.
- [87] O. Ronneberger, P. Fischer, and T. Brox, “U-net: Convolutional networks for biomedical image segmentation,” in *MICCAI*. Springer, 2015, pp. 234–241.
- [88] M. Yang, K. Yu, C. Zhang, Z. Li, and K. Yang, “Denseaspp for semantic segmentation in street scenes,” in *CVPR*, 2018, pp. 3684–3692.
- [89] R. Dong, X. Pan, and F. Li, “Denseu-net-based semantic segmentation of small objects in urban remote sensing images,” *IEEE Access*, vol. 7, pp. 65 347–65 356, 2019.
- [90] A. Kirillov, R. Girshick, K. He, and P. Dollár, “Panoptic feature pyramid networks,” in *CVPR*, 2019, pp. 6392–6401.
- [91] G. Lin, A. Milan, C. Shen, and I. Reid, “Refinenet: Multi-path refinement networks for high-resolution semantic segmentation,” in *CVPR*, 2017, pp. 5168–5177.
- [92] L.-C. Chen, G. Papandreou, F. Schroff, and H. Adam, “Rethinking atrous convolution for semantic image segmentation,” *arXiv preprint arXiv:1706.05587*, 2017.
- [93] X. Li, Z. Zhong, J. Wu, Y. Yang, Z. Lin, and H. Liu, “Expectation-maximization attention networks for semantic segmentation,” in *ICCV*, 2019, pp. 9166–9175.
- [94] Y. Yuan, L. Huang, J. Guo, C. Zhang, X. Chen, and J. Wang, “Ocnet: Object context network for scene parsing,” *arXiv preprint arXiv:1809.00916*, 2018.
- [95] Z. Huang, X. Wang, L. Huang, C. Huang, Y. Wei, and W. Liu, “Cnet: Criss-cross attention for semantic segmentation,” in *ICCV*, 2019, pp. 603–612.
- [96] H. Zhang, K. Dana, J. Shi, Z. Zhang, X. Wang, A. Tyagi, and A. Agrawal, “Context encoding for semantic segmentation,” in *CVPR*, 2018, pp. 7151–7160.
- [97] K. Sun, Y. Zhao, B. Jiang, T. Cheng, B. Xiao, D. Liu, Y. Mu, X. Wang, W. Liu, and J. Wang, “High-resolution representations for labeling pixels and regions,” *arXiv preprint arXiv:1904.04514*, 2019.
- [98] L. Mou, Y. Hua, and X. X. Zhu, “A relation-augmented fully convolutional network for semantic segmentation in aerial scenes,” in *CVPR*, 2019, pp. 12 416–12 425.
- [99] Z. Huang, Y. Wei, X. Wang, W. Liu, T. S. Huang, and H. Shi, “Alignseg: Feature-aligned segmentation networks,” *IEEE Trans. Pattern Anal. Mach. Intell.*, vol. 44, no. 1, pp. 550–557, 2022.
- [100] Y. Yuan, X. Chen, and J. Wang, “Object-contextual representations for semantic segmentation,” in *ECCV*. Springer, 2020, pp. 173–190.
- [101] R. Niu, X. Sun, Y. Tian, W. Diao, K. Chen, and K. Fu, “Hybrid multiple attention network for semantic segmentation in aerial images,” *IEEE Trans. Geosci. Remote Sens.*, vol. 60, pp. 1–18, 2022.
- [102] Z. Zheng, Y. Zhong, J. Wang, and A. Ma, “Foreground-aware relation network for geospatial object segmentation in high spatial resolution remote sensing imagery,” in *CVPR*, 2020, pp. 4095–4104.

- [103] A. Ma, J. Wang, Y. Zhong, and Z. Zheng, "Factseg: Foreground activation-driven small object semantic segmentation in large-scale remote sensing imagery," *IEEE Trans. Geosci. Remote Sens.*, vol. 60, pp. 1–16, 2022.
- [104] S. Ren, K. He, R. Girshick, and J. Sun, "Faster r-cnn: Towards real-time object detection with region proposal networks," *IEEE Trans. Pattern Anal. Mach. Intell.*, vol. 39, no. 6, pp. 1137–1149, June 2017.
- [105] T.-Y. Lin, P. Goyal, R. Girshick, K. He, and P. Dollár, "Focal loss for dense object detection," *IEEE Trans. Pattern Anal. Mach. Intell.*, vol. 42, no. 2, pp. 318–327, 2020.
- [106] Z. Chen, J. Zhang, and D. Tao, "Recursive context routing for object detection," *Int. J. Comput. Vis.*, vol. 129, no. 1, pp. 142–160, 2021.
- [107] G.-S. Xia, X. Bai, J. Ding, Z. Zhu, S. Belongie, J. Luo, M. Datcu, M. Pelillo, and L. Zhang, "Dota: A large-scale dataset for object detection in aerial images," in *CVPR*, June 2018.
- [108] Z. Liu, L. Yuan, L. Weng, and Y. Yang, "A high resolution optical satellite image dataset for ship recognition and some new baselines," in *ICPRAM*, 2017, pp. 324–331.
- [109] X. Xie, G. Cheng, J. Wang, X. Yao, and J. Han, "Oriented r-cnn for object detection," in *ICCV*, October 2021, pp. 3520–3529.
- [110] "Aerialdetection," <https://github.com/dingjiansw101/AerialDetection>.
- [111] Q. Ming, Z. Zhou, L. Miao, H. Zhang, and L. Li, "Dynamic anchor learning for arbitrary-oriented object detection," in *AAAI*, vol. 35, no. 3, 2021, pp. 2355–2363.
- [112] W. Qian, X. Yang, S. Peng, J. Yan, and Y. Guo, "Learning modulated loss for rotated object detection," *AAAI*, vol. 35, no. 3, pp. 2458–2466, May 2021.
- [113] X. Yang, J. Yan, Z. Feng, and T. He, "R3det: Refined single-stage detector with feature refinement for rotating object," *AAAI*, vol. 35, no. 4, pp. 3163–3171, May 2021.
- [114] J. Han, J. Ding, J. Li, and G.-S. Xia, "Align Deep Features for Oriented Object Detection," *IEEE Trans. Geosci. Remote Sens.*, vol. 60, p. 3062048, Jan. 2022.
- [115] S. M. Azimi, E. Vig, R. Bahmanyar, M. K'orner, and P. Reinartz, "Towards multi-class object detection in unconstrained remote sensing imagery," in *ACCV*. Springer, 2018, pp. 150–165.
- [116] G. Zhang, S. Lu, and W. Zhang, "CAD-Net: A Context-Aware Detection Network for Objects in Remote Sensing Imagery," *IEEE Trans. Geosci. Remote Sens.*, vol. 57, no. 12, pp. 10 015–10 024, Dec. 2019.
- [117] J. Ding, N. Xue, Y. Long, G.-S. Xia, and Q. Lu, "Learning roi transformer for oriented object detection in aerial images," in *CVPR*, 2019, pp. 2844–2853.
- [118] X. Yang, J. Yang, J. Yan, Y. Zhang, T. Zhang, Z. Guo, X. Sun, and K. Fu, "Scrdet: Towards more robust detection for small, cluttered and rotated objects," in *ICCV*, 2019, pp. 8231–8240.
- [119] Y. Xu, M. Fu, Q. Wang, Y. Wang, K. Chen, G.-S. Xia, and X. Bai, "Gliding vertex on the horizontal bounding box for multi-oriented object detection," *IEEE Trans. Pattern Anal. Mach. Intell.*, vol. 43, no. 4, pp. 1452–1459, 2021.
- [120] C. Li, C. Xu, Z. Cui, D. Wang, T. Zhang, and J. Yang, "Feature-attentioned object detection in remote sensing imagery," in *ICIP*, 2019, pp. 3886–3890.
- [121] S. Zhang, C. Chi, Y. Yao, Z. Lei, and S. Z. Li, "Bridging the gap between anchor-based and anchor-free detection via adaptive training sample selection," in *CVPR*, 2020, pp. 9756–9765.
- [122] K. Fu, Z. Chang, Y. Zhang, and X. Sun, "Point-based estimator for arbitrary-oriented object detection in aerial images," *IEEE Trans. Geosci. Remote Sens.*, vol. 59, no. 5, pp. 4370–4387, 2021.
- [123] J. Wang, J. Ding, H. Guo, W. Cheng, T. Pan, and W. Yang, "Mask OBB: A Semantic Attention-Based Mask Oriented Bounding Box Representation for Multi-Category Object Detection in Aerial Images," *Remote Sens.*, vol. 11, no. 24, p. 2930, Dec. 2019.
- [124] Z. Zhang, W. Guo, S. Zhu, and W. Yu, "Toward Arbitrary-Oriented Ship Detection With Rotated Region Proposal and Discrimination Networks," *IEEE Geosci. Remote Sens. Lett.*, vol. 15, no. 11, pp. 1745–1749, Nov. 2018.
- [125] M. Liao, Z. Zhu, B. Shi, G.-s. Xia, and X. Bai, "Rotation-sensitive regression for oriented scene text detection," in *CVPR*, 2018, pp. 5909–5918.
- [126] T. Zhang, X. Zhang, P. Zhu, P. Chen, X. Tang, C. Li, and L. Jiao, "Foreground refinement network for rotated object detection in remote sensing images," *IEEE Trans. Geosci. Remote Sens.*, vol. 60, pp. 1–13, 2022.
- [127] Y. Jiang, X. Zhu, X. Wang, S. Yang, W. Li, H. Wang, P. Fu, and Z. Luo, "R2cnn: Rotational region cnn for orientation robust scene text detection," *arXiv preprint arXiv:1706.09579*, 2017.
- [128] J. Ma, W. Shao, H. Ye, L. Wang, H. Wang, Y. Zheng, and X. Xue, "Arbitrary-oriented scene text detection via rotation proposals," *IEEE Trans. Multimedia*, vol. 20, no. 11, pp. 3111–3122, 2018.
- [129] X. Zhang, G. Wang, P. Zhu, T. Zhang, C. Li, and L. Jiao, "Grs-det: An anchor-free rotation ship detector based on gaussian-mask in remote sensing images," *IEEE Trans. Geosci. Remote Sens.*, vol. 59, no. 4, pp. 3518–3531, 2021.
- [130] M. A. Lebedev, Y. V. Vizilter, O. V. Vygolov, V. A. Knyaz, and A. Y. Rubis, "Change Detection in Remote Sensing Images Using Conditional Adversarial Networks," *Int. Arch. Photogrammetry, Remote Sens. Spatial Inf. Sci.*, vol. 422, pp. 565–571, May 2018.
- [131] H. Chen and Z. Shi, "A spatial-temporal attention-based method and a new dataset for remote sensing image change detection," *Remote Sens.*, vol. 12, no. 10, 2020.
- [132] S. Ji, S. Wei, and M. Lu, "Fully convolutional networks for multisource building extraction from an open aerial and satellite imagery data set," *IEEE Trans. Geosci. Remote Sens.*, vol. 57, no. 1, pp. 574–586, 2019.
- [133] H. Chen, Z. Qi, and Z. Shi, "Remote Sensing Image Change Detection With Transformers," *IEEE Trans. Geosci. Remote Sens.*, vol. 60, p. 3095166, Jan. 2022.
- [134] R. Caye Daudt, B. Le Saux, and A. Boulch, "Fully convolutional siamese networks for change detection," in *ICIP*, 2018, pp. 4063–4067.
- [135] Z. Zheng, Y. Wan, Y. Zhang, S. Xiang, D. Peng, and B. Zhang, "CLNet: Cross-layer convolutional neural network for change detection in optical remote sensing imagery," *ISPRS J. Photogramm. Remote Sens.*, vol. 175, pp. 247–267, May 2021.
- [136] S. Fang, K. Li, J. Shao, and Z. Li, "SNUNet-CD: A Densely Connected Siamese Network for Change Detection of VHR Images," *IEEE Geosci. Remote Sens. Lett.*, vol. 19, p. 3056416, Jan. 2022.
- [137] C. Zhang, P. Yue, D. Tapete, L. Jiang, B. Shangguan, L. Huang, and G. Liu, "A deeply supervised image fusion network for change detection in high resolution bi-temporal remote sensing images," *ISPRS J. Photogramm. Remote Sens.*, vol. 166, pp. 183–200, Aug. 2020.
- [138] J. Chen, Z. Yuan, J. Peng, L. Chen, H. Huang, J. Zhu, Y. Liu, and H. Li, "DASNet: Dual Attentive Fully Convolutional Siamese Networks for Change Detection in High-Resolution Satellite Images," *IEEE J. Sel. Topics Appl. Earth Observ. Remote Sens.*, vol. 14, pp. 1194–1206, Jan. 2021.
- [139] M. Liu, Q. Shi, A. Marinoni, D. He, X. Liu, and L. Zhang, "Super-Resolution-Based Change Detection Network With Stacked Attention Module for Images With Different Resolutions," *IEEE Trans. Geosci. Remote Sens.*, vol. 60, p. 3091758, Jan. 2022.
- [140] H. Du, Y. Zhuang, S. Dong, C. Li, H. Chen, B. Zhao, and L. Chen, "Bilateral Semantic Fusion Siamese Network for Change Detection From Multitemporal Optical Remote Sensing Imagery," *IEEE Geosci. Remote Sens. Lett.*, vol. 19, p. 3082630, Jan. 2022.
- [141] Q. Shi, M. Liu, S. Li, X. Liu, F. Wang, and L. Zhang, "A deeply supervised attention metric-based network and an open aerial image dataset for remote sensing change detection," *IEEE Trans. Geosci. Remote Sens.*, vol. 60, pp. 1–16, 2022.
- [142] X. Hou, Y. Bai, Y. Li, C. Shang, and Q. Shen, "High-resolution triplet network with dynamic multiscale feature for change detection on satellite images," *ISPRS J. Photogramm. Remote Sens.*, vol. 177, pp. 103–115, Jul. 2021.
- [143] H. Chen, W. Li, and Z. Shi, "Adversarial Instance Augmentation for Building Change Detection in Remote Sensing Images," *IEEE Trans. Geosci. Remote Sens.*, vol. 60, p. 3066802, Jan. 2022.
- [144] W. G. C. Bandara and V. M. Patel, "A transformer-based siamese network for change detection," *arXiv preprint arXiv:2201.01293*, 2022.
- [145] Q. Ke and P. Zhang, "CS-HSNet: A Cross-Siamese Change Detection Network Based on Hierarchical-Split Attention," *IEEE J. Sel. Topics Appl. Earth Observ. Remote Sens.*, vol. 14, pp. 9987–10 002, Jan. 2021.
- [146] H. Lee, K. Lee, J. H. Kim, Y. Na, J. Park, J. P. Choi, and J. Y. Hwang, "Local Similarity Siamese Network for Urban Land Change Detection on Remote Sensing Images," *IEEE J. Sel. Topics Appl. Earth Observ. Remote Sens.*, vol. 14, pp. 4139–4149, Jan. 2021.
- [147] Z. Zheng, A. Ma, L. Zhang, and Y. Zhong, "Change is everywhere: Single-temporal supervised object change detection in remote sensing imagery," in *ICCV*, 2021, pp. 15 173–15 182.